

# **Pattern Formation in Spatially Forced Systems: Application to Vegetation Restoration**

Thesis submitted in partial fulfillment  
of the requirements for the degree of  
“DOCTOR OF PHILOSOPHY”

by

**Yair Mau**

Submitted to the Senate of  
Ben-Gurion University of the Negev

October 14, 2013

Beer-Sheva

# Pattern Formation in Spatially Forced Systems: Application to Vegetation Restoration

Thesis submitted in partial fulfillment  
of the requirements for the degree of  
“DOCTOR OF PHILOSOPHY”

by

**Yair Mau**

Submitted to the Senate of  
Ben-Gurion University of the Negev

Approved by the advisor

Approved by the Dean of the Kreitman School of Advanced Graduate Studies

October 14, 2013

Beer-Sheva

This work was carried out under the supervision of

*Prof. Ehud Meron*

In the Department of Physics

Faculty of Natural Sciences

Ben-Gurion University of the Negev

I, Yair Mau, whose signature appears below, hereby declare that

---- I have written this Thesis by myself, except for the help and guidance offered by my Thesis Advisors.

---- The scientific materials included in this Thesis are products of my own research, culled from the period during which I was a research student.

---- This Thesis incorporates research materials produced in cooperation with others, excluding the technical help commonly received during experimental work. Therefore, I am attaching another affidavit stating the contributions made by myself and the other participants in this research, which has been approved by them and submitted with their approval.

Date:

Student's name:

Signature:

---

## Acknowledgments

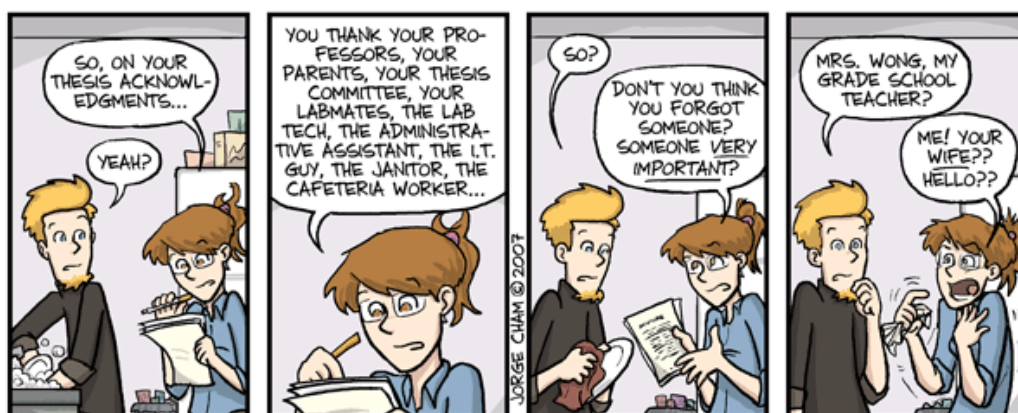
During my doctorate I have been time and again reminded that knowing something and explaining it meaningfully to someone else are two very different things. I hope that this thesis succeeds in bridging the gap, and I would like to acknowledge those who helped me, for I couldn't have done it alone. These people accompanied me in this journey, teaching me, discussing ideas, and giving me much needed support.

I offer my sincerest gratitude to my advisor, Prof. Ehud Meron, for his guidance, patience, and support. I gained much from his knowledge and creative thinking, and specially for teaching me to see the story behind the equations and simulations.

I would like to thank my research colleagues, Aric Hagberg, Lev Haim, Shai Kinast, Yuval Zelnik and Yonatan Natan. We had so many great discussions together, we promiscuously exchanged notes and computer codes, and I surely learned more from them than from most university courses I ever took. It has been fun, thank you! A special note of appreciation to Lev Haim, my academic brother in arms, with whom I could discuss our daily advances (and retreats), and some of the topics presented in this thesis are the result of a fruitful collaboration between us.

I am indebted to many more people, who have had a positive influence on me during my PhD. Among them I will mention my office colleagues Eitan Rothstein, Mahary Vasioun and Sarit Nagar, the cartoonists Zach Weinersmith, Randall Munroe and Jorge Cham (see cartoon next page), and the composers Ludwig van Beethoven and James Booker.

Finally, I would like to thank my parents, my sisters and my grandparents. You always gave me strength and confidence, and I hope I have made you proud. My loving wife, Liat, gave me the greatest gift one can receive, 1.5 years ago, our daughter Yaara. I dedicate this thesis to both of you.



WWW.PHDCOMICS.COM

# Contents

<b>Abstract</b>	<b>6</b>
<b>1 Introduction</b>	<b>8</b>
<b>2 Background</b>	<b>13</b>
2.1 The Swift-Hohenberg equation . . . . .	13
2.1.1 Linear stability analysis . . . . .	14
2.1.2 Periodic solutions . . . . .	16
2.1.3 The parametrically forced SH equation . . . . .	17
2.1.4 Multiple scales analysis . . . . .	19
2.1.5 Resonant 2d patterns . . . . .	21
2.2 Vegetation . . . . .	24
2.2.1 The BWH model . . . . .	24
2.2.2 Dimensions and parameter values . . . . .	27
2.2.3 A brief review of earlier model studies . . . . .	28
<b>3 Resonant stripe patterns</b>	<b>31</b>
3.1 Multiple scales analysis . . . . .	32
3.1.1 Scaling . . . . .	32
3.1.2 Order $ \epsilon ^{1/2}$ . . . . .	32
3.1.3 Order $ \epsilon $ . . . . .	33
3.1.4 Order $ \epsilon ^{3/2}$ . . . . .	34
3.1.5 Amplitude equation . . . . .	34
3.2 Uniform and stationary solutions . . . . .	34

## CONTENTS

---

<b>4</b>	<b>Interference of 2d patterns</b>	<b>39</b>
4.1	Multiple scales analysis . . . . .	41
4.1.1	Scaling . . . . .	41
4.1.2	Order $ \epsilon ^{1/4}$ . . . . .	43
4.1.3	Order $ \epsilon ^{2/4}$ . . . . .	43
4.1.4	Order $ \epsilon ^{3/4}$ . . . . .	43
4.1.5	Order $ \epsilon ^{4/4}$ . . . . .	45
4.1.6	Order $ \epsilon ^{5/4}$ . . . . .	45
4.1.7	Amplitude equations . . . . .	46
4.2	Uniform and stationary solutions . . . . .	47
4.3	Stability analysis of stripe patterns . . . . .	48
4.4	Functional competition . . . . .	51
<b>5</b>	<b>Vegetation</b>	<b>54</b>
5.1	The simplified vegetation model . . . . .	56
5.1.1	Turning off the root-augmentation feedback . . . . .	58
5.1.2	Turning off the shading feedback . . . . .	59
5.1.3	Simplified equations and rescaling . . . . .	59
5.2	Spatially periodic forcing . . . . .	61
5.3	Uniform solutions . . . . .	61
5.4	Linear stability analysis . . . . .	62
5.5	1d solutions . . . . .	63
5.6	2d solutions . . . . .	64
5.6.1	Patterns outside their stability range . . . . .	66
5.6.2	Front dynamics . . . . .	71
5.7	Preventive measures . . . . .	76
5.8	Comparison with the SH model . . . . .	79
<b>6</b>	<b>Conclusion</b>	<b>82</b>
<b>A</b>	<b>Semi-spectral method for PDEs</b>	<b>85</b>
A.1	The method . . . . .	85
A.2	Step by step . . . . .	87
A.3	Example . . . . .	88



# List of Figures

2.1	Dispersion relation of the SH equation . . . . .	15
2.2	The neutral stability curve . . . . .	15
2.3	1d solution of the SH equation . . . . .	16
2.4	Evolution of a 2d pattern . . . . .	17
2.5	Rectangular and oblique patterns. . . . .	18
2.6	Spectrum of the rectangular pattern. . . . .	22
2.7	The infiltration function. . . . .	27
2.8	Bifurcation graph of uniform vegetation solutions. . . . .	29
2.9	Sequence of vegetation states. . . . .	30
3.1	Existence domains of $n : 1$ resonant stripes in 1d. . . . .	36
3.2	1d wavenumber-locked solutions. . . . .	38
4.1	Existence domains of 2d patterns . . . . .	40
4.2	Two bistable solutions in 2d. . . . .	41
4.3	Existence and stability of $1 : 1$ resonant stripes. . . . .	51
4.4	Lyapunov functional for different solutions. . . . .	53
4.5	Front dynamics between bistable solutions. . . . .	53
5.1	Stages of rehabilitation of vegetation. . . . .	55
5.2	Self-organized vegetation patterns. . . . .	56
5.3	The periodically forced infiltration contrast. . . . .	61
5.4	Bifurcation graph of uniform and patterned solutions. . . . .	64
5.5	Bifurcation graph of wavenumber-locked vegetation solutions. . . . .	66
5.6	Evolution of stripe pattern outside its stability range. . . . .	67
5.7	Evolution of rectangular pattern outside its stability range. . . . .	68

## LIST OF FIGURES

---

5.8	Rectangular and stripe patterns taken out of their stability ranges. . . . .	69
5.9	Collapse of a stripe pattern outside its stability range. . . . .	70
5.10	Tangential and normal fronts of rectangular and bare soil, $p = 0.80$ . . . . .	73
5.11	Tangential and normal fronts of rectangular and stripe patterns, $p = 0.89$ . . . . .	75
5.12	Tangential and normal fronts of rectangular pattern and bare soil, $p = 0.89$ . . . . .	75
5.13	Tangential and normal fronts of stripe pattern and bare soil, $p = 0.89$ . . . . .	77
5.14	Tangential and normal fronts of stripe pattern and bare soil, $p = 0.95$ . . . . .	77
5.15	Mean biomass versus precipitation, for rectangular and stripe patterns. . . . .	78
5.16	Rectangular patterns for different values of $k_f$ . . . . .	80
5.17	Rectangular patterns of the SH and vegetation models. . . . .	81

# List of Tables

5.1	Parameters of the <i>BWH</i> vegetation model . . . . .	57
5.2	Values of the non-dimensional parameters of the simplified vegetation model. . . . .	60

## Abstract

Spatial periodic forcing can entrain a pattern-forming system in the same way as temporal periodic forcing can entrain an oscillator. The forcing can lock the pattern's wavenumber to a fraction of the forcing wavenumber within tongue-like domains in the forcing parameter plane; it can increase the pattern's amplitude and also create patterns below their onset.

In this dissertation we study two pattern-forming systems subjected to parametric periodic forcing in space. First we take the Swift-Hohenberg equation, a very simple system that produces static periodic solutions. We wish to understand how pattern-forming systems in general respond to parametric forcing, and for that purpose we derive amplitude equations for wavenumber-locked states in one and two dimensions. We find that in one space dimension, the forcing is always able to increase the stability region of patterned solutions in the parameter space, even in regions below the threshold of pattern formation of the unforced system. In two-dimensional domains, we find that the system can respond to one-dimensional forcing by creating two-dimensional oblique and rectangular patterns. These patterns can dramatically reduce the stability range of stripe patterns, even when the forcing wavenumber is equal to the system's natural wavenumber. Stable stripe patterns can also be displaced by oblique and rectangular patterns, due to the lower energy functional of the latter.

We also study the rehabilitation of damaged vegetation in water-limited regions. Water-harvesting techniques are used to recover these ecological systems, such as the construction of periodic topography modulations on a hill slope, that accumulate runoff, and along which trees are planted. Because vegetation in water limited regions can self-organize in periodic patterns, the spatial modulations can be understood as spatial periodic forcing applied to a pattern forming system. We develop a simple mathematical model for vegetation in drylands, and introduce to it a parametric forcing that imitates the role of the spatial modulation. We find two kinds of wavenumber-locked

---

solutions: stripe patterns in a  $1 : 1$  resonance with the forcing wavenumber, and rectangular patterns in a  $2 : 1$  resonance. The rectangular pattern extends to lower precipitation values and is found to be more resilient than the stripe pattern, because it easily adapts itself to climatic changes. The stripe pattern, when taken out of its stability region, can cause a partial, or even complete, collapse of the vegetation system. In addition to that, the rectangular pattern can displace bare soil and stripe solutions, which is a significant result regarding the reversal of desertification. The displacement of bare soil by the rectangular pattern means that spatial periodic forcing renders desertification reversible, and even relatively small vegetation patches can slowly expand and dominate the whole domain. This kind of reaction is called gradual regime shift, in opposition to large and abrupt changes which characterize catastrophic shifts.

Finally, we conclude this dissertation by reviewing the main results presented. The recasting of rehabilitation of vegetation systems as a problem of spatial periodic forcing can yield important preventive measures against desertification. One procedure can be the removal of vegetation from a resonant  $1 : 1$  stripe solution, so it can resemble the resilient rectangular configuration, and thus avoid the collapse of vegetation when environmental changes take place. We believe that the study of parametric forcing on simple pattern forming systems and on more complex physical systems can be very fruitful. Simpler systems lend themselves to deeper mathematical analysis, whose results shed light on more complex systems. The study of more complex systems in turn can raise new general questions to be investigated with simpler systems.

**Keywords:** pattern formation, self-organization, parametric forcing, vegetation patterns, ecosystem rehabilitation.



# Chapter 1

## Introduction

*“It is only slightly overstating the case to say that physics is the study of symmetry.”*

– Philip. W. Anderson

Pattern formation phenomena are found in a wide variety of physical, chemical, and biological contexts. Examples include embryonic pattern formation [1, 2], cardiac arrhythmias [3], bacterial colonies [4, 5], nano-particle assemblies [6], two-phase mixtures [7], thermal convection [8], nonlinear optics [9], chemical [10] and electrochemical reactions [11], and environmental pattern formation [12, 13, 14]. In some contexts pattern formation is essential for the functioning of the system. This is the case with embryonic pattern formation or with vegetation patterning — a mechanism by which vegetation copes with water stress. In other contexts pattern formation is an undesired outcome. This is the case with spiral waves in the heart muscle [15], dewetting of liquid films [16], or spatial patterning in the transverse directions of a laser beam [17]. In order to eliminate, modify or induce patterns, means of controlling and manipulating them are needed. These means may consist of basic parameter tuning, or may involve external intervention, such as feedback control [18], or periodic forcing in time [19] and space [20, 21, 22, 23].

Temporal periodic forcing of an oscillatory system is a classical problem. An early realization is Kapitza’s pendulum [24] — a rigid pendulum with



a pivot point that is forced to vibrate in the vertical direction. When the vibration, or forcing frequency, is sufficiently high the unstable upper vertical position of the pendulum can be controlled and stabilized. Another control aspect of this and other examples of forced oscillations, including spatially extended systems, is frequency locking. An oscillatory system subjected to time-periodic (spatially uniform) forcing is capable of changing its oscillation frequency,  $\omega$ , to lock at a fraction of the forcing frequency,  $\omega_f$ , provided this fraction is close enough to the natural frequency  $\omega_0$  of the unforced system. The frequency locking, or entrainment, capability increases with the forcing strength, at least for relatively weak forcing. As a consequence, in the parameter plane spanned by the forcing strength and frequency, the entrainment occurs in a tongue-like domain, often called an Arnold tongue. Mathematically, if  $\omega_f$  is close to  $(n/m)\omega_0$ , where  $n, m \in \mathbb{Z}$ , there exists a domain in the forcing parameter plane — the  $n:m$  resonance tongue, within which the actual oscillation frequency can be controlled by varying the forcing frequency according to  $\omega = (m/n)\omega_f$ .

Numerous examples of oscillatory systems entrained by periodic temporal forcing exist. Entrainment of mammalian circadian rhythms by the day-night periodicity is one class of examples [25]. Additional physiological examples include entrainment of the heart rate [26], of the respiratory phase [27], and of insulin and glucose oscillations [28]. Many more examples can be found in areas as varied as chemistry [29, 30, 31, 32] and optics [33, 34].

There are two additional signatures of periodically forced oscillatory systems that relate to frequency locking. The first is multiplicity of stable oscillation states sharing the same frequency but differing in oscillation phase. Associated with this multi-stability are front structures and rich pattern-formation phenomena, [35, 36, 37, 38, 32, 31], including traveling waves that restrict the domain of resonant nonuniform oscillations [39]. The second signature is the possible generation of a symmetry-breaking instability by the periodic forcing. This instability can lead to  $2:1$  frequency-locked standing-wave patterns even outside the  $2:1$  resonance tongue of uniform oscillations. This is a reflection of the freedom of a spatially extended oscillatory system to resonate with a spatially uniform time-periodic forcing



by forming spatial patterns that change the oscillation frequency through dispersion [40, 41, 42].

Spatial forcing of a pattern-forming system is analogous to temporal forcing of an oscillating system; the system can respond to the forcing by locking its wavenumber  $k$  to the forcing wavenumber  $k_f$ . That is, for any  $k_f$  close enough to  $(n/m)k_0$ , where  $n, m \in \mathbb{Z}$  and  $k_0$  is the system's natural wavenumber, the system can respond with a wavenumber  $k = (m/n)k_f$ . In the forcing parameter plane (forcing strength versus forcing frequency) wavenumber-locked or resonant patterns occupy tongue-like domains - the spatial analogs of Arnold tongues. Within such tongues the wavenumbers of resonant patterns are controllable by tuning the forcing wavenumber. Spatially forced pattern-forming systems have been studied in various contexts including nematic liquid crystals [20, 43], light-sensitive chemical reactions [22], Rayleigh-Bénard convection [21, 44], liquid crystal light valve optical systems [45], and bottom formation in slightly meandering channels [46].

The analogy to temporally forced oscillations extends also to the two additional signatures of periodic forcing, multi-stability of phase states and fronts [47], and a symmetry-breaking instability induced by a one-dimensional (1d) spatially periodic forcing. In this case, the instability breaks the remaining symmetry in the direction orthogonal to the spatial forcing, and leads to resonant two-dimensional (2d) rectangular or oblique patterns [48, 49, 44]. The patterns are wavenumber-locked to the forcing in a 2:1 resonance and extend far beyond the boundaries of the 2:1 resonant tongue of stripe patterns to a range that includes the 1:1 resonance ( $k_f \approx k_0$ ). The wide resonance range of the 2d patterns is a consequence of the development of a wave-vector component in the direction orthogonal to the forcing that compensates for the unfavorable wavenumber  $k_f/2$  in the forcing direction.

The basic 1:1 resonance of stripe patterns is generally the first choice for inducing, stabilizing, or controlling stripe patterns. This is the case, in restoring degraded vegetation in water-limited landscapes by periodic arrays of micro-catchments that concentrate surface runoff and form favorable conditions for vegetation growth in a fluctuating environment [50]. However, the influence of 2d patterns on 1:1 stripe patterns has not yet been studied. In





this thesis we use a simple pattern-formation model – the Swift-Hohenberg model – to study the interaction between  $1 : 1$  resonant stripes and  $2 : 1$  resonant rectangular and oblique patterns, and the extent to which the 2d patterns interfere with the control of the resonant stripe patterns.

We then study the problem of recovery of vegetation in degraded drylands. Climatic variations and human activity can cause reduction or loss of biological productivity, process which is called *desertification*. Quite often, when environmental conditions of a damaged vegetation system return to their previous state, the vegetation is unable to recover spontaneously, because of the multiple stability of unproductive and productive states. Water-harvesting techniques can be used to reverse desertification, and make the degraded area productive again. A major restoration practice is the construction of periodic arrays of parallel dikes that intercept and accumulate runoff, and thereby locally increase the soil-water content. We develop a simple vegetation model for water-limited systems, and introduce to it spatial periodic forcing that imitates the role of the parallel dikes. Since vegetation in drylands has the tendency of self-organizing in patches with a characteristic wavelength, often in the form of parallel stripes perpendicular to the slope direction, the planting of vegetation along these dikes can be successful as long as the model admits  $1 : 1$  wavenumber locked solutions.

The structure of the dissertation is as follows: Chapter 2 summarizes some of the mathematical tools of pattern formation theory, using the Swift-Hohenberg model as an example. We discuss known results of 2d resonant solutions of the parametrically forced Swift-Hohenberg equation [48, 49], which will be useful in later chapters. We also review a vegetation model [51] and some of its results. In Chapter 3 we work with the one-dimensional parametrically forced Swift-Hohenberg equation, and we derive amplitude equations for its  $n : 1$  resonant solutions. Chapter 4 deals with the interaction of  $1 : 1$  stripe solutions with the 2d resonant patterns presented in the Background. With the help of amplitude equations for these two solutions, we study the effects of the 2d patterns on the stability of the  $1 : 1$  stripes. We also use the energy functional to find ranges in the parameter space where stripe and 2d patterns compete and can displace one another. Chapter 5 presents a sim-



## Chapter 1. Introduction

---

plified version of the vegetation model presented in the Background, and we add to it spatial parametric forcing. We discuss in which situations different kinds of resonant solutions are more suitable, and we propose measures that aim to maximize the success of the rehabilitation in changing environmental conditions. Finally, in Chapter 6 we summarize the main findings of this thesis, discuss their validity in the context of the models' limitations, and suggest future research directions.



# Chapter 2

## Background

*“Essentially, all models are wrong, but some are useful.”*

– George E. P. Box

### 2.1 The Swift-Hohenberg equation

The Swift-Hohenberg (SH) equation was introduced in 1977 as an approximation of the behavior of the Rayleigh–Bénard convection near the onset of convective motion [52]. The physical system consists of a fluid bounded by infinite horizontal plates separated by a distance  $\ell$ , with a fixed temperature difference  $\Delta T$  between them. The partial differential equation below describes the evolution of the dimensionless scalar quantity  $u$ , which is a function of the fluid velocity in the vertical direction and the deviation of the temperature from the gradient  $\Delta T/\ell$ :

$$\partial_t u = \epsilon u - u^3 - (\nabla^2 + k_0^2)^2 u \quad (2.1)$$

Since its debut, the SH equation has become a canonical model of many kinds of systems that produce stationary periodic patterns, not necessarily related to the convection problem, such as lasers [53], oscillons in granular media [54] and ecosystem modelling [55]. Its simplicity makes it easily modifiable in order to study the basic properties of different pattern-forming



systems.

### 2.1.1 Linear stability analysis

It is easy to see that  $u_0 = 0$  is a stationary solution of the equation above, and we call it the *zero solution*. In order to study its stability to nonuniform perturbations, we substitute

$$u = u_0 + \delta e^{\sigma t + ikx} + \delta^* e^{\sigma t - ikx} \quad (2.2)$$

into Equation (2.1) and keep only linear terms in  $\delta$  and  $\delta^*$ . Grouping terms by their exponents, we obtain the dispersion relation

$$\sigma(k) = \epsilon - (k_0^2 - k^2)^2, \quad (2.3)$$

which describes how the growth rate  $\sigma$  of the perturbation depends on its wavenumber  $k$ . Figure 2.1 shows three curves of the dispersion relation, for values of  $\epsilon$  smaller, equal and larger than zero. For  $\epsilon < 0$  the growth rate is negative for all values of  $k$ , meaning that the perturbation will decay in time, and therefore  $u_0$  is stable. For  $\epsilon = 0$  we find a critical value  $k_0$  of the perturbation wavenumber, for which  $\sigma = 0$ . As  $\epsilon$  becomes positive, a perturbation with wavenumber  $k_0$  will be the first to grow, and destabilize the zero solution. For  $\epsilon > 0$ , there is a whole band of modes for which  $\sigma(k) > 0$  that will grow. This is the basic mechanism of a *finite wavenumber instability*.

When we take Equation (2.3) to be zero, we have the *neutral stability curve*

$$\epsilon(k) = (k_0 - k^2)^2, \quad (2.4)$$

which divides the parameter space  $(\epsilon, k)$  in two regions, where  $u_0$  is stable and unstable. Figure 2.2 shows in gray shade the region where the zero solution is unstable, and in the region in white this solution is stable. We can see that as  $\epsilon$  increases beyond zero, the band of modes with wavenumber  $k$  becomes wider. Because of random fluctuations, even if we perturb  $u_0$  with

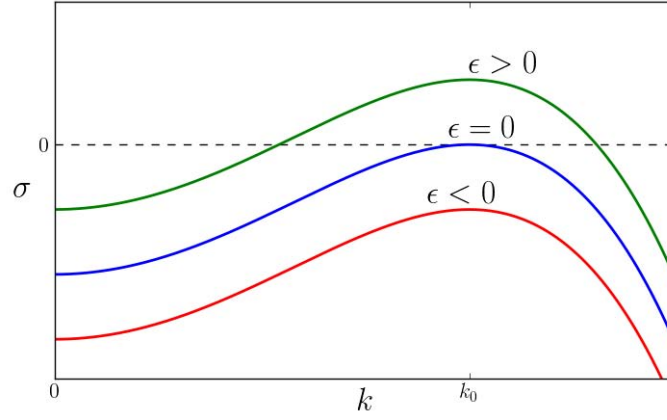


Figure 2.1: Dispersion relation of the zero solution of the SH equation.

a wavenumber  $k$  outside the instability region, eventually a wavenumber from within the range will develop and make the zero solution unstable. Therefore, we see again in Figure 2.2 that only for  $\epsilon < 0$  all perturbations decay. From now on we will refer to  $\epsilon_c = 0$  as the critical value, the bifurcation point, or threshold value.

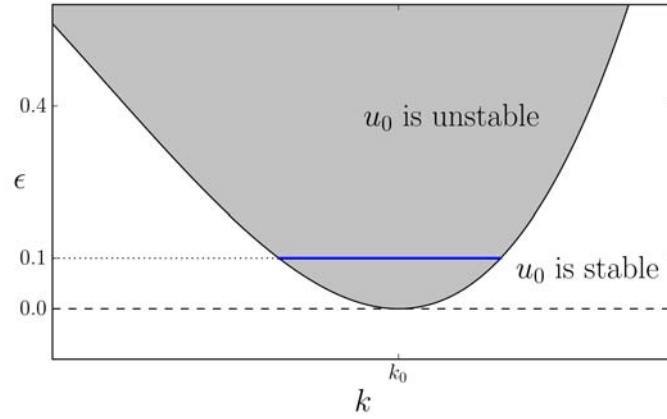


Figure 2.2: The neutral stability curve. The white (gray) area denotes a stable (unstable) zero solution. The band in blue shows the range of wavenumber values that make  $u_0$  unstable, for  $\epsilon = 0.1$ .



### 2.1.2 Periodic solutions

For  $0 < \epsilon \ll 1$  we expect only perturbations with wavenumber  $k$  in the range

$$k_0 - \frac{\sqrt{\epsilon}}{2k_0} < k < k_0 + \frac{\sqrt{\epsilon}}{2k_0} \quad (2.5)$$

to grow from a zero solution, resulting in a ‘cosine-like’ pattern. Indeed, when we simulate Equation (2.1) in one spatial dimension we get a typical pattern as shown in Figure 2.3, with a typical wavelength of  $\lambda_0 = 2\pi/k_0$ .

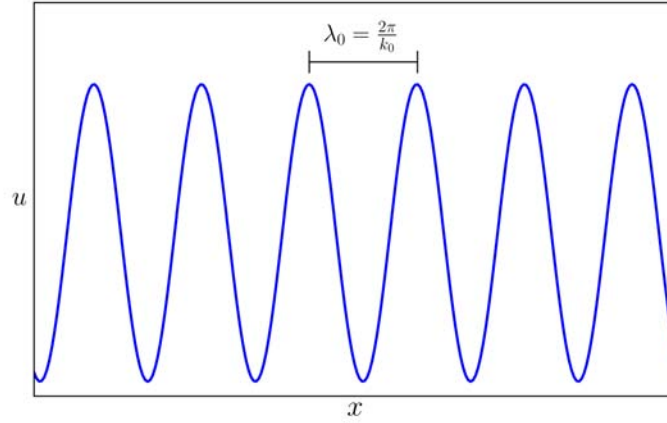


Figure 2.3: Steady state of a 1d simulation of Equation (2.1) with random initial conditions. Parameters:  $\epsilon = 0.1$ ,  $k_0 = 1$ .

In two space dimensions a stripe pattern develops above the instability threshold. Figure 2.4 shows a simulation with random initial conditions. Because of space isotropy, the system initially contains domains of stripe patterns in different directions. Eventually defects in the pattern are resolved, and the whole system ends up as one single pattern of parallel stripes.

The evolution of the system can be understood in ‘free energy’ terms. The Swift-Hohenberg equation is a variational system, because Equation (2.1) can be rewritten as

$$\partial_t u = -\frac{\delta F}{\delta u}, \quad (2.6)$$

where  $F$  is called *Lyapunov functional*, and  $\delta$  denotes the variational derivative. It is easy to show that  $\partial_t F < 0$ , and therefore the evolution of the

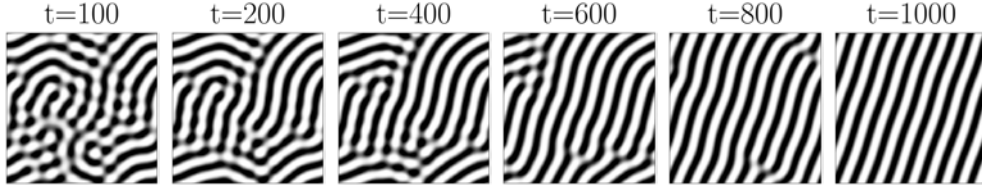


Figure 2.4: A 2d simulation of Equation (2.1) with random initial conditions. Parameters:  $\epsilon = 0.1$ ,  $k_0 = 1$ .

system is such that the value of  $F$  decreases monotonically. From this property of  $F$ , we also call it free energy, in analogy with the behavior of the free energy in thermodynamic systems. For the SH equation, the Lyapunov functional reads

$$F = \int d\mathbf{r} \left( -\frac{1}{2}\epsilon u^2 + \frac{1}{4}u^4 + \frac{1}{2}(\nabla^2 u + k_0^2 u)^2 \right). \quad (2.7)$$

### 2.1.3 The parametrically forced SH equation

In order to study the effects of spatial periodic forcing on pattern forming systems, we can take the model presented above, and add a forcing term to it. This can be done in several ways, and we choose in this thesis to deal only with parametric forcing of the linear term. As we will discuss in detail in Chapter 5, water-harvesting techniques modulate the growth rate of vegetation, which makes them a form of parametric forcing. We would like the forced SH equation to show the qualitative features of periodically forced pattern-forming systems, like the vegetation system, and this is the reason for the specific choice of forcing.

We modify Equation (2.1) by modulating the control parameter  $\epsilon$  periodically in space, in the  $x$  direction only. The parametrically forced Swift-Hohenberg equation reads

$$\partial_t u = [\epsilon + \gamma \cos(k_f x)] u - u^3 - (\nabla^2 + k_0^2)^2 u, \quad (2.8)$$

where  $\gamma$  is the forcing strength and  $k_f$  is the forcing wavenumber.

Simulating the equation above in 2d, starting from random initial con-



ditions, one can find two new kinds of patterns in the range  $0 < k_f < 2k_0$ . For  $\gamma > \epsilon$  we find rectangular patterns, and for  $\gamma < \epsilon$  oblique patterns. By looking at the absolute value of their Fourier transforms in Figure 2.5, we find that the periodicity of both patterns in the  $x$  direction is controlled by the wavenumber  $k_x$  of size  $k_f/2$ . In addition to that, the wavenumber in the perpendicular direction,  $k_y$ , is such that the overall wavevector is of length  $k_0$ . This means that both patterns are wavenumber-locked solutions, because as the forcing wavenumber  $k_f$  is changed,  $k_x$  changes accordingly, always keeping the exact relation  $k_x = k_f/2$ .

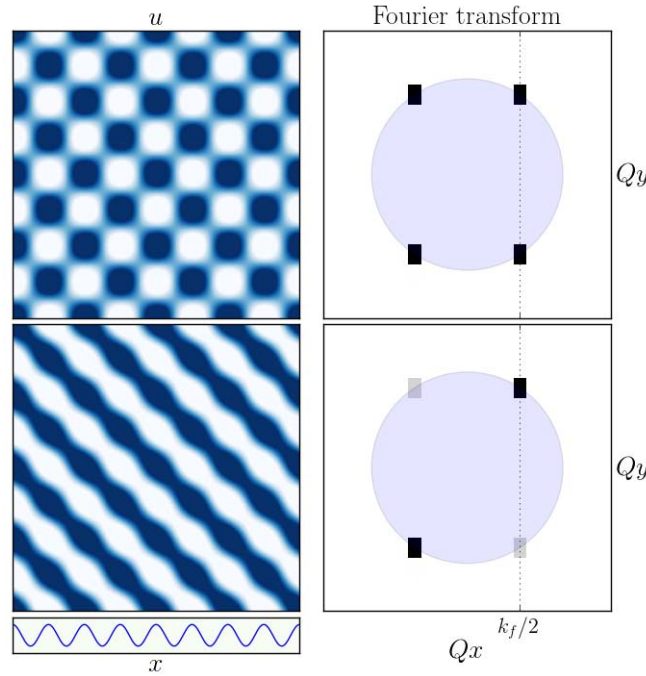


Figure 2.5: Two dimensional solutions of Equation (2.8). On the top left a rectangular pattern ( $\gamma = 0.2$ ), and below it an oblique pattern ( $\gamma = 0.05$ ). The panels on the right show the patterns' respective Fourier transform absolute value, where the circle in blue has radius  $k_0$ . The short box on the lower left indicates the periodic forcing in  $x$ . Parameters:  $\epsilon = 0.1$ ,  $k_f = 1.1$ ,  $k_0 = 1.0$ .

The wavenumber-locked solutions above are in a  $2 : 1$  resonance with the forcing (a  $n : m$  resonance means that  $nk_x = mk_f$ ). In order to understand these resonant solutions better, we will make use of the multiple time-scales





analysis, as explained below. We will follow the analysis developed by Manor et al. [48, 49]. But before the actual analysis, a few words on the technique used.

### 2.1.4 Multiple scales analysis

The multiple scales analysis is a perturbative method that helps us describe the evolution of a given mode that develops near an instability point. Let's say we have a general dynamical system

$$\partial_t \mathbf{u} = \mathbf{f}(\mathbf{u}, \partial_x, \lambda), \quad (2.9)$$

where  $\mathbf{u}$  is a vector of  $n$  dependent variables,  $\mathbf{f}$  is a function of the components of the variables vector  $\mathbf{u}$ , their spatial derivatives, and of the control parameter  $\lambda$ . Near the instability point  $\lambda_c$ , the variables can be expanded as the power series

$$\mathbf{u} = \epsilon^p \mathbf{u}_1 + \epsilon^{2p} \mathbf{u}_2 + \epsilon^{3p} \mathbf{u}_3 + \dots, \quad (2.10)$$

where  $\epsilon = (\lambda - \lambda_c)/\lambda_c \ll 1$  denotes the distance to the instability point, and the power  $p$  can be determined by balancing the different terms in  $\mathbf{f}$ . For instance, taking Equation (2.8) as an example,  $\epsilon_c = 0$  is the critical value, therefore  $\epsilon$  itself can be used in the power series. By requiring that the terms  $\epsilon u$  and  $u^3$  balance each other, we find that  $u \sim \epsilon^{1/2}$ , so we have that  $p = 1/2$ .

The multiple time-scales analysis assumes that near the instability point the dynamics depend on several weak time and space scales. They are defined as  $T_i = \epsilon^q t$  and  $X_i = \epsilon^r x$ , and again the powers  $q$  and  $r$  are determined by balancing terms in  $\mathbf{f}$ . In the case of Equation (2.8), balancing terms  $\partial_t u$  and  $\epsilon u$  yields  $\partial_t \sim \epsilon$ , therefore  $q = 1$ . Balancing terms  $\epsilon u$  and  $-2k_0^2 \nabla^2 u$  yields  $\nabla^2 \sim \epsilon$ , therefore  $r = 1/2$ .

The partial derivatives in (2.9) can also be expanded according to the



chain rule:

$$\begin{aligned}\frac{\partial}{\partial t} &= \sum_{i=0}^{\infty} \frac{\partial}{\partial T_i} \frac{\partial T_i}{\partial t} = \partial_t + \epsilon^q \partial_{T_1} + \epsilon^{2q} \partial_{T_2} + \dots \\ \frac{\partial}{\partial x} &= \sum_{i=0}^{\infty} \frac{\partial}{\partial X_i} \frac{\partial X_i}{\partial x} = \partial_x + \epsilon^r \partial_{X_1} + \epsilon^{2r} \partial_{X_2} + \dots\end{aligned}\tag{2.11}$$

The perturbation method consists in substituting Equations (2.10) and (2.11) into Equation (2.9) and grouping terms by their order of  $\epsilon$ . Order  $i$  looks like

$$\mathcal{L} \mathbf{u}_i = \mathbf{RHS}_i,\tag{2.12}$$

where the operator  $\mathcal{L}$  is an  $n \times n$  matrix, and  $\mathbf{RHS}_i$  denotes all the terms on the *right-hand side*, and it is a function of all  $\mathbf{u}_j$  for  $j < i$ . For each order,  $\mathbf{u}_i$  must be solved. Furthermore, to avoid secular terms that make  $\mathbf{u}_i$  diverge, we have to apply the Fredholm alternative, as explained below:

- We define an inner product  $(f, g)$ . For instance, if we are making the analysis near a finite wavenumber instability with critical wavenumber  $k_0$ , a reasonable choice is

$$(f, g) = \frac{1}{\ell} \int_0^\ell f^*(x) g(x) dx, \quad \ell = \frac{2\pi}{k_0}\tag{2.13}$$

- We find the adjoint operator  $\mathcal{L}^\dagger$ , where

$$(\mathcal{L}f, g) = (f, \mathcal{L}^\dagger g)\tag{2.14}$$

- We find the kernel  $\mathbf{h}$  of  $\mathcal{L}^\dagger$ :  $\mathcal{L}^\dagger \mathbf{h} = 0$ .
- Finally, we require that  $(\mathbf{RHS}_i, \mathbf{h}) = 0$ , i.e. the right-hand side must be orthogonal to the nullspace  $\mathbf{h}$ . This requirement yields constraints, which are called *solvability conditions*, and they guarantee that  $\mathbf{u}_i$  is free of secular terms.

In the first order  $i = 1$  to be solved, we have to *assume* the lowest-order approximation  $\mathbf{u}_1$ . The linear stability analysis of Equation (2.9) gives us



hints of what kinds of basic states to choose. For example, we have seen in Subsections 2.1.1 and 2.1.2 that the unforced Swift-Hohenberg equation forms stripe-like patterns when  $\epsilon > 0$ . If we want to study these stripe solutions, we can choose as a first-order approximation  $u_1 = A(X_i, T_i) \exp(ik_0 x) + c.c.$ , where *c.c.* denotes *complex conjugate*. The choice must be of modes that describe the solution we want to study (e.g. stripe solutions), weakly modulated by amplitude functions.

We iteratively solve for each  $\mathbf{u}_i$ , and the solvability condition for each order gives dynamic equations for the modulating amplitudes. When sufficient terms  $\mathbf{u}_i$  have been found (according to one's discretion), all equations of the amplitudes can be joined in one single set of *Amplitude Equations*.

### 2.1.5 Resonant 2d patterns

We will now derive amplitude equations for the rectangular and oblique modes shown in Figure 2.5. We assume that  $|\epsilon| \ll 1$ , and we expand  $u$  as a power series:

$$u = |\epsilon|^{1/2} u_1 + |\epsilon|^{2/2} u_2 + |\epsilon|^{3/2} u_3 + \dots \quad (2.15)$$

We take  $u_1$ , the lowest order approximation, to be

$$u_1 = a(X, Y, T) e^{i(k_x x + k_y y)} + b(X, Y, T) e^{i(k_x x - k_y y)} + c.c., \quad (2.16)$$

where  $a$  and  $b$  are complex amplitudes that are functions of ‘slow’ space and time variables  $X$ ,  $Y$ , and  $T$ . The choice of  $u_1$  is based on the Fourier transform of the rectangular and oblique patterns. In Figure 2.6 we see a typical Fourier transform of a rectangular pattern. All four vectors  $\pm \vec{k}_1$  and  $\pm \vec{k}_2$  were represented in Equation (2.16).

The independent variables scale as  $X = |\epsilon|^{1/2} x$ ,  $Y = |\epsilon|^{1/2} y$  and  $T = |\epsilon| t$ , so the time and space derivatives will now read

$$\partial_x \rightarrow \partial_x + |\epsilon|^{1/2} \partial_X, \quad \partial_y \rightarrow \partial_y + |\epsilon|^{1/2} \partial_Y, \quad \partial_t \rightarrow |\epsilon| \partial_T. \quad (2.17)$$



## Chapter 2. Background

Note that because  $u_1$  does not depend on the fast time scale  $t$ , the time derivative will be substituted by derivatives regarding slower time scales only.

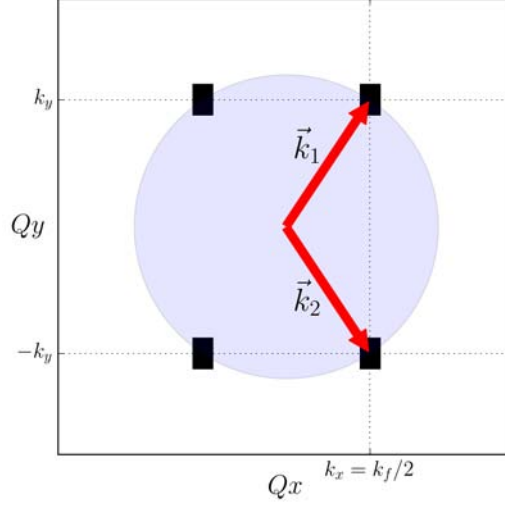


Figure 2.6: Fourier transform of the rectangular pattern shown in Figure 2.5. The two vectors in red have coordinates  $\vec{k}_1 = (k_x, k_y)$  and  $\vec{k}_2 = (k_x, -k_y)$ . The circle in blue has radius  $k_0$ .

We substitute Equations (2.15) and (2.17) into Equation (2.8), and take the forcing strength to be  $\gamma = |\epsilon| \Gamma$ . We group terms of the same order of  $\epsilon$  and solve each equation separately.

**Order  $|\epsilon|^{1/2}$**

We have that

$$\mathcal{L}u_1 = 0, \quad (2.18)$$

where  $\mathcal{L} = (\partial_x^2 + \partial_y^2 + k_0^2)^2$ . Equation (2.16) satisfies Equation (2.18), with the condition that  $k_x^2 + k_y^2 = k_0^2$ . This means that both modes of the lowest order approximation have wavevectors of length  $k_0$ .

**Order  $|\epsilon|^{2/2}$**

$$\mathcal{L}u_2 = 0. \quad (2.19)$$



## Chapter 2. Background

---

This order looks exactly as the previous order, and no new information will be gained here. We therefore assume  $u_2 = 0$ .

**Order  $|\epsilon|^{3/2}$**

$$\mathcal{L}u_3 = -\partial_T u_1 + u_1 - u_1^3 - 4(\partial_x \partial_X + \partial_y \partial_Y)^2 u_1 + \Gamma u_1 \cos(k_f x). \quad (2.20)$$

When substituting  $u_1$  into the equation above, we have to identify the resonant terms, i.e., those terms that have exponents of the kind  $\exp(\pm i k_x x \pm i k_y y)$ . In order to avoid secular terms in  $u_3$ , we have to apply the solvability condition, which means setting the coefficients of these exponents to zero. This yields dynamical equations for the amplitudes  $a$  and  $b$ , and thus we call the result *amplitude equations*. We would like the lowest order terms to be wavenumber locked in a 2 : 1 resonance with the forcing wavenumber, so we substitute  $k_f = 2k_x$  in (2.20). The solvability condition gives

$$\begin{aligned} \partial_T a &= a - 3(|a|^2 + 2|b|^2)^2 a + 4(k_x \partial_X + k_y \partial_Y)^2 a + \frac{\Gamma}{2} b^* \\ \partial_T b &= b - 3(2|a|^2 + |b|^2)^2 b + 4(k_x \partial_X - k_y \partial_Y)^2 b + \frac{\Gamma}{2} a^*. \end{aligned} \quad (2.21)$$

### Amplitude Equations

Going back to the ‘fast’ variables  $x$ ,  $y$  and  $t$ , and rescaling  $\Gamma = |\epsilon|^{-1}\gamma$ ,  $a = |\epsilon|^{-1/2}\tilde{a}$  and  $b = |\epsilon|^{-1/2}\tilde{b}$ , we get, after taking out the superscript tilde:

$$\begin{aligned} \partial_t a &= \epsilon a - 3(|a|^2 + 2|b|^2)^2 a + 4(k_x \partial_x + k_y \partial_y)^2 a + \frac{\gamma}{2} b^* \\ \partial_t b &= \epsilon b - 3(2|a|^2 + |b|^2)^2 b + 4(k_x \partial_x - k_y \partial_y)^2 b + \frac{\gamma}{2} a^*. \end{aligned} \quad (2.22)$$

Because of the rescaling of  $a$  and  $b$  above,  $u$  is now seen as

$$u = a e^{i(k_x x + k_y y)} + b e^{i(k_x x - k_y y)} + c.c. + h.o.t., \quad (2.23)$$

where *h.o.t* are *higher order terms*.



## Uniform and Stationary Solutions

The amplitude equations (2.22) admit two uniform and stationary stable solutions. The rectangular solution reads

$$a_0 = \rho_0 e^{i\alpha}, \quad b_0 = \rho_0 e^{-i\alpha}, \quad \rho_0 = \sqrt{\frac{\epsilon + \frac{\gamma}{2}}{3}}, \quad (2.24)$$

where  $\alpha$  is an arbitrary phase. The oblique solution reads

$$a_{\pm} = \rho_{\pm} e^{i\alpha}, \quad b_{\mp} = \rho_{\mp} e^{-i\alpha}, \quad \rho_{\pm} = \sqrt{\frac{\epsilon \pm \sqrt{\epsilon^2 - \gamma^2}}{6}}. \quad (2.25)$$

The rectangular and oblique solutions look like the patterns shown in Figure 2.5, and they are stable for a very wide range of  $k_f$ .

## 2.2 Vegetation

Many kinds of vegetation patterns, such as stripes, spots, labyrinth, gaps and others, have been observed in arid and semi-arid regions around the world [56, 57, 58, 59, 60, 61]. Water is the most constraining resource for those systems, and the patterns formed can be the result of several positive feedbacks between the biomass and water. The feedbacks are responsible for redistributing water in the system, which breaks spatial symmetry and can lead to the formation of patterns.

In the last 15 years many models of biomass-water interactions have been proposed to explain the abundance of vegetation patterns seen in nature [62, 63, 64, 65, 66, 67, 68, 69]. In this thesis we will work with a simplified version of the model introduced by Gilad et al., which we present below.

### 2.2.1 The BWH model

The model describes the evolution of three dynamical variables:  $B(\mathbf{X}, T)$  is the above-ground biomass of the vegetation;  $W(\mathbf{X}, T)$  is the soil-water available to the plants; and  $H(\mathbf{X}, T)$  is the surface water. All dynamic variables



are densities measured in  $\text{kg}/\text{m}^2$ . The equations read

$$\partial_T B = G_B B (1 - B/K) - MB + D_B \hat{\nabla}^2 B \quad (2.26a)$$

$$\partial_T W = \mathcal{I}H - LW - G_W W + D_W \hat{\nabla}^2 W \quad (2.26b)$$

$$\partial_T H = P - \mathcal{I}H + 2D_H \hat{\nabla} \cdot \left[ H \left( \hat{\nabla} H + \hat{\nabla} Z \right) \right], \quad (2.26c)$$

where the time and space scales of the derivatives  $\partial_T$  and  $\hat{\nabla}$  are years and meters, respectively. In equation (2.26a),  $G_B$  is a biomass growth function,  $K$  is the maximum standing biomass,  $M$  is the mortality rate, and  $D_B$  is the seed dispersal rate. In equation (2.26b),  $\mathcal{I}$  is the infiltration function,  $L$  is the evaporation function,  $G_W$  represents the soil-water consumption rate, and  $D_W$  is the soil-water diffusion rate. In equation (2.26c),  $P$  is the mean annual precipitation rate, and the last term describes the flow of the surface water on a topography function  $Z$ , and it originates from shallow water theory. Let us examine in more detail some of the components in Equations (2.26) and the roles they play in the different feedbacks.

### Root-augmentation feedback

Both  $G_B$  and  $G_W$  are integrals defined as

$$G_B(\mathbf{X}, T) = \Lambda \int_{\Omega} \mathcal{G}(\mathbf{X}, \mathbf{X}', T) W(\mathbf{X}', T) d\mathbf{X}' \quad (2.27a)$$

$$G_W(\mathbf{X}, T) = \Gamma \int_{\Omega} \mathcal{G}(\mathbf{X}', \mathbf{X}, T) B(\mathbf{X}', T) d\mathbf{X}' \quad (2.27b)$$

$$\mathcal{G}(\mathbf{X}, \mathbf{X}', T) = \frac{1}{2\pi S_0^2} \exp \left[ -\frac{|\mathbf{X} - \mathbf{X}'|^2}{2S_0^2 (1 + EB(\mathbf{X}, T))^2} \right]. \quad (2.27c)$$

$G_B$  represents the soil-water that the plant's root system is able to draw from the ground. The kernel  $\mathcal{G}$  is a function of  $S_0$ , the minimal root system size, of the root augmentation per unit biomass  $E$ , and of biomass  $B$ . The integration is performed on the whole domain, but the Gaussian center is at the plant's position.

$G_W$  represents the soil-water consumption, and it also uses the same kernel  $\mathcal{G}$ , albeit with reversed prime tagging. This makes a great difference:



the water consumption in a given point is affected by the root system of all plants in that point's vicinity.

The root-augmentation feedback mechanism is the following: a plant with access to soil water has increased growth rate, and that makes the root system grow according to  $EB$  in the kernel function. A greater root system means that more soil water becomes available to the plant, which enhances its growth even further.

### Shading feedback

The evaporation function  $L$  is given by

$$L(\mathbf{X}, T) = \frac{N}{\left(1 + \frac{RB(\mathbf{X}, T)}{K}\right)}, \quad (2.28)$$

where  $N$  is the evaporation rate in bare soil, and  $R$  represents the reduction in evaporation of soil-water due to the plant's presence. More biomass means a greater shading effect on evaporation, which makes more water available to the plant, which in turn allows it to grow even further.

### Infiltration feedback

The infiltration function  $\mathcal{I}$  reads

$$\mathcal{I}(\mathbf{X}, T) = A \frac{B(\mathbf{X}, T) + Qf}{B(\mathbf{X}, T) + Q}. \quad (2.29)$$

When the biomass is zero, we have the infiltration rate of bare soil:  $\mathcal{I} = Af$ . For large biomass values ( $B \gg Q$ ), we have the infiltration rate of a fully vegetated state:  $\mathcal{I} = A$ . The parameter  $f$  is bounded between 0 and 1, and it regulates the contrast in infiltration: when  $f$  is large there is little contrast in infiltration between the bare soil and the fully vegetated state, and vice-versa. The parameter  $Q$  represents a reference biomass beyond which the plant approaches its full capacity to increase the infiltration rate. Figure 2.7 depicts the infiltration function dependence on the biomass.

A biological soil crust is responsible for this contrast in infiltration. The



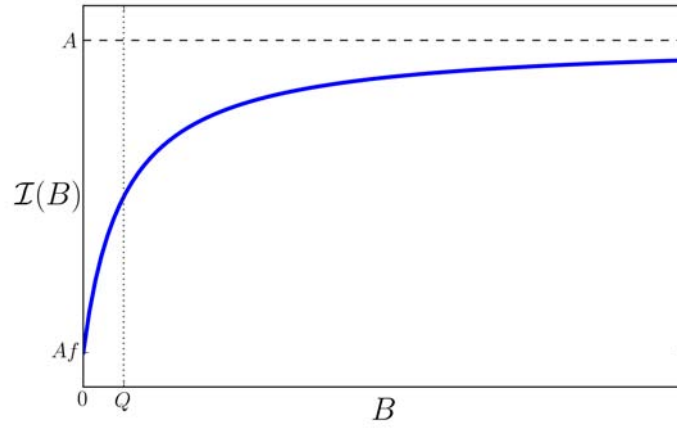


Figure 2.7: The infiltration as a function of the biomass.

bare soil surface is often made of a matrix of soil crust, covered with a microphytic community of cyanobacteria, bacteria, and other microorganisms [70]. The cyanobacteria and bacteria excrete polysaccharides that glue together soil particles and make the crust flat and solid, and as a result the water infiltration rate is greatly diminished. The biological crust, though, cannot develop under patches of vegetation because the vegetation and the litter it produces block sunlight, and thus the infiltration rate in these patches is greater than it is in bare soil covered by biological crust. This contrast in the infiltration rate of runoff produces a positive feedback, where a small patch will act as a sink, attracting more water and resulting in an even larger vegetation patch.

### 2.2.2 Dimensions and parameter values

All three dynamical variables  $B$ ,  $W$  and  $H$  are densities, measured in  $\text{kg}/\text{m}^2$ . We can use the density of water  $\rho_h = 10^3 \text{kg}/\text{m}^3$  to define a new surface water variable  $\mathcal{H}$ :

$$H \left[ \frac{\text{kg}}{\text{m}^2} \right] = \rho_h \left[ \frac{\text{kg}}{\text{m}^3} \right] \times \mathfrak{h}[\text{m}] = \cancel{\rho_h} \left[ \frac{\text{kg}}{\text{m}^3} \right] \times \cancel{10^{-3}} \mathcal{H}[\text{mm}] = \mathcal{H}[\text{mm}], \quad (2.30)$$

where the square brackets indicate the dimensions of the variable, and  $\mathfrak{h}$  is the height of the surface water in meters. The above result means that



whatever quantity related to water measured in  $[\text{kg m}^{-2}]$  can also be measured in millimeters, without any conversion parameter. This goes for  $P$ , which can also be understood as the precipitation rate in  $\text{mm} [\text{yr}^{-1}]$ . The quantity  $Z$  is actually  $Z = \rho_h \zeta$ , where  $\zeta$  is the topography function in meters.

### 2.2.3 A brief review of earlier model studies

The model presented above is capable of reproducing qualitatively many features of vegetation systems in drylands. Figure 2.8 shows two bifurcation diagrams, of the biomass as a function of precipitation, for different solutions of Equations (2.26). The bifurcation graph on the top shows only the uniform bare soil solution  $\mathcal{B}$  and uniform-cover solution  $\mathcal{E}$ . The bare soil solution is stable for  $P < P_c$ , and above  $P_c$  it becomes unstable and a uniform cover branch appears in a subcritical bifurcation. The uniform cover solution itself undergoes a finite wavenumber instability at  $P = P_2$ . For  $P_1 < P < P_2$  the uniform cover solution is unstable to nonuniform perturbations, and becomes stable for  $P > P_2$ . The graph on the bottom shows the same two uniform solutions (but now the uniform cover is called  $\mathcal{V}$ ), with the addition of a spot-pattern branch  $\mathcal{S}$ . This branch is stable down to  $P = P_0$ . The bifurcation graph shows that when precipitation is decreased below  $P_0$ , the spot-pattern collapses to the bare soil solution. Even when precipitation returns to higher values, the system continues on the stable bare soil solution. The BWH model presented above can successfully reproduce a desertification scenario because it contains a bistability range of a productive state and an unproductive state (the range is  $P_0 < P < P_c$  for the graph on the bottom).

What kinds of patterned solutions does the BWH model yield? At the bifurcation point  $P = P_2$  in the top graph of Figure 2.8, a new solution branch appears, representing a patterned state (the branch is not shown). Near the bifurcation point, the patterned state has a characteristic wavelength. Depending on the parameters and the initial conditions, the system admits three basic kinds of patterned solutions, in addition to the uniform bare soil and the uniform cover solutions: vegetation spots, stripes and gaps. Figure 2.9 shows a sequence of five solutions to the system, as the precipitation

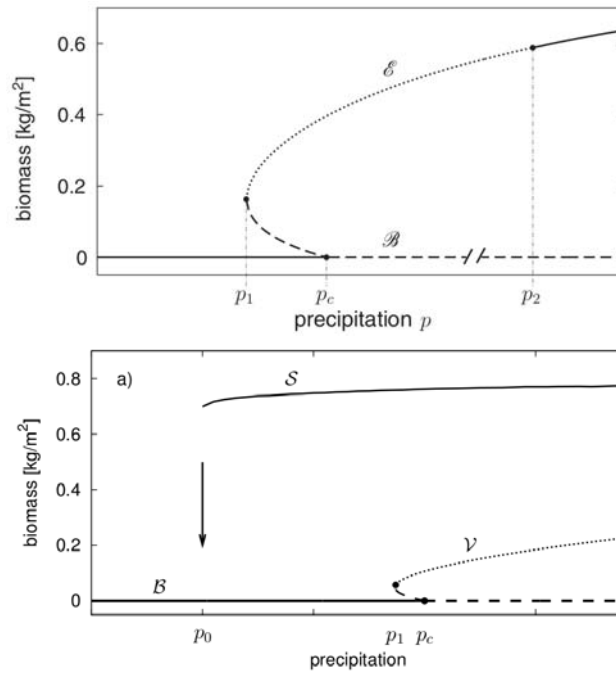


Figure 2.8: Bifurcation graph of uniform solutions of Equations (2.26). The graph on the top shows two branches of uniform solutions, the bare soil solution  $\mathcal{B}$  and the uniform cover solution  $\mathcal{E}$ . The graph on the bottom shows an additional branch  $\mathcal{S}$ , that corresponds to a spot-pattern solution. Full lines denote stability, while broken lines indicate instability. The graph on the top was taken from [51], and the one on the bottom was taken from [71].

rate is increased, from left to right (panels ‘a’ through ‘e’). Each of the five states has its stability range, and neighboring solutions often overlap their stability regions, making possible mixed solutions (panels ‘f’ through ‘i’). The multiple stability of solutions effectively makes the number of possible configurations infinite.

In flat and horizontal terrain, the stripe pattern does not have any preferred direction along which it can orient itself, and the pattern looks like a labyrinth. In flat and inclined terrain, a hill slope, space isotropy is broken, and there is a clear preferred direction. The vegetation self-organizes in parallel stripes perpendicular to the gradient of the slope. An intuitive explanation for this specific orientation is to imagine that if the stripes were along the slope’s gradient, the runoff would just pass between them, and the

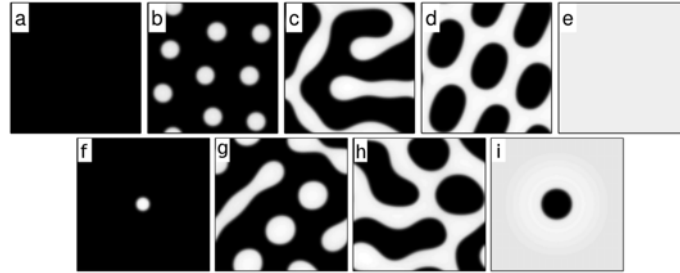


Figure 2.9: Panels ‘a’ through ‘e’ show five kinds of solutions of (2.26) for increasing precipitation rate values, from left to right: bare soil, spots, stripes, gaps, and uniform cover. Panels ‘f’ through ‘i’ show combinations of neighboring bistable solutions. Figure adapted from [72].

vegetation would not profit from this configuration. By aligning themselves perpendicular to the gradient, the vegetation stripes are able to make the most of the runoff. In fact, one should expect the upper part of a stripe to benefit more from runoff than the part of the stripe that is slightly downhill. This is exactly the case: the vegetation at the top is able to expand uphill, and the vegetation on the bottom dies from lack of water. Thus, the parallel stripes on a hill slope were found to travel uphill [51].



## Chapter 3

# Resonant stripe patterns

*“Physics is mathematical not because we know so much about the physical world, but because we know so little; it is only its mathematical properties that we can discover.”*

– Bertrand Russell

We wish to find resonant stripe pattern solutions for the 1d parametrically forced Swift-Hohenberg equation

$$\partial_t u = [\epsilon + \gamma \cos(k_f x)] u - u^3 - (\partial_x^2 + k_0^2)^2 u. \quad (3.1)$$

We assume that the forcing wavenumber,  $k_f$ , is close to a multiple of  $k_0$ , that is

$$k_f \approx nk_0, \quad n \in \mathbb{Z}, \quad (3.2)$$

and let  $\nu$  be the deviation or detuning from exact resonance:

$$\nu = k_0 - k_f/n. \quad (3.3)$$

The solution family of the unforced system that spans the wavenumber range (2.5) can increase the freedom of the system to resonate with the forcing. This is because for any forcing wavenumber  $k_f$ , such that  $k_f/n$  is within the range (2.5), there exists a solution of the unforced system with that particular wavenumber. The forcing can further increase the resonance range by



creating stripe solutions with wavenumbers outside the range (2.5). Resonant solutions are said to be *wavenumber locked* because they react to the forcing with a wavenumber  $k$  which is exactly equal to  $k_f/n$ , for an  $n : 1$  resonance. In order to study these solutions, we will now derive amplitude equations using the multiple scales analysis.

## 3.1 Multiple scales analysis

### 3.1.1 Scaling

Consider the case of weak forcing ( $\gamma \ll 1$ ) near the instability of the zero solution ( $|\epsilon| \ll 1$ ). The stripe solutions that appear beyond the instability point have small amplitudes that vary slowly in time and space. We thus expand solutions of Equation (3.1) as

$$u = \sum_{i=1}^{\infty} |\epsilon|^{i/2} u_i(x_0, x_1, t_1), \quad (3.4)$$

where  $x_i = |\epsilon|^{i/2} x$  ( $i = 0, 1$ ) and  $t_1 = |\epsilon| t$  are the slow space and time variables. We further expand the forcing strength as

$$\gamma = \sum_{i=1}^{\infty} |\epsilon|^{i/2} \gamma_i, \quad \gamma_i \sim O(1), \quad (3.5)$$

and assume the scaling  $\nu \sim |\epsilon|^{1/2}$  for the small detuning. With these choices of the slow space and time variables the derivatives in (3.1) transform according to:

$$\partial_x = \partial_{x_0} + |\epsilon|^{1/2} \partial_{x_1}, \quad \partial_t = |\epsilon| \partial_{t_1}. \quad (3.6)$$

### 3.1.2 Order $|\epsilon|^{1/2}$

Substituting Equations (3.4)–(3.6) into Equation (3.1) we find at order  $|\epsilon|^{1/2}$

$$\mathcal{L}^2 u_1 = 0, \quad (3.7)$$



where  $\mathcal{L} = (\partial_{x_0}^2 + k_0^2)$ . The solution of this equation can be written as

$$u_1 = a(x_1, t_1) e^{ik_0 x_0} + c.c., \quad (3.8)$$

where the amplitude  $a$  depends on the slow variables  $x_1$  and  $t_1$ .

### 3.1.3 Order $|\epsilon|$

At order  $|\epsilon|$  we find

$$\begin{aligned} \mathcal{L}^2 u_2 &= \frac{\gamma_1}{2} (e^{ik_f x_0} + e^{-ik_f x_0}) u_1 \\ &= \frac{\gamma_1}{2} (a e^{i(k_f+k_0)x_0} + a^* e^{i(k_f-k_0)x_0}) + c.c.. \end{aligned} \quad (3.9)$$

Solvability of (3.9) requires the elimination of secular terms from the right hand side of the equation. The secular terms are those in which the fast spatial dependence is described by the harmonic factor  $e^{\pm ik_0 x_0}$ . For all resonances  $n \neq 2$  the right hand side does not contain secular terms and no solvability condition has to be imposed. For  $n = 2$ , however, there are secular terms,  $e^{\pm i(k_f-k_0)x_0}$ , since  $k_f \cong 2k_0$ . To eliminate the secular terms we must set  $\gamma_1 = 0$  for the 2:1 resonance. We accomplish this condition by multiplying  $\gamma_1$  by  $1 - \delta_{n,2}$ , where  $\delta_{i,j}$  is the Kronecker delta. The general solution of (3.9) is a superposition of a particular solution and a general solution of the homogeneous problem:

$$\begin{aligned} u_2 &= (1 - \delta_{n,2}) \frac{\gamma_1}{2} \left[ d_+ a e^{i(k_f+k_0)x_0} + d_- a^* e^{i(k_f-k_0)x_0} \right] \\ &\quad + c(x_1, x_2, t_1, t_2, \dots) e^{ik_0 x_0} + c.c., \end{aligned} \quad (3.10)$$

where

$$d_{\pm} = \frac{1}{k_f^2 (k_f \pm 2k_0)^2}. \quad (3.11)$$



### 3.1.4 Order $|\epsilon|^{3/2}$

Finally, at order  $|\epsilon|^{3/2}$  we find

$$\begin{aligned} \mathcal{L}^2 u_3 = & u_1 - u_1^3 - \partial_{t_1} u_1 - \mathcal{M}^2 u_1 - 2\mathcal{M}\mathcal{L}u_2 \\ & + \frac{1}{2} (e^{ik_f x_0} + e^{-ik_f x_0}) (\gamma_2 u_1 + \gamma_1 u_2), \end{aligned} \quad (3.12)$$

where  $\mathcal{M} = 2\partial_{x_0}\partial_{x_1}$ . In order to identify the secular terms we insert the solutions Equations (3.8) and (3.10) for  $u_1$  and  $u_2$  into the right hand side of Equation (3.12) and note that since the detuning is of order  $|\epsilon|^{1/2}$  we can write  $k_f x_0 = n(k_0 x_0 - \nu_1 x_1)$ , where  $\nu_1 = |\epsilon|^{-1/2}\nu \sim O(1)$ . Summing up all contributions to the secular terms and setting their coefficients to zero gives

$$\begin{aligned} a_{t_1} = & a - 3|a|^2 a + (2k_0)^2 \partial_{x_1}^2 a + \delta_{n,2} \frac{\gamma_2}{2} a^* \\ & + (1 - \delta_{n,2}) \left( \frac{\gamma_1}{2} \right)^2 [\eta_1 a + \delta_{n,1} d_- e^{-2i\nu_1 x_1} a^*], \end{aligned} \quad (3.13)$$

where  $\eta_1 = d_+ + d_-$ .

### 3.1.5 Amplitude equation

Introducing the amplitude variable  $A = |\epsilon|^{1/2} e^{i\nu_1 x_1} a$ , and going back to the fast time and space variables, we obtain the amplitude equation

$$\begin{aligned} A_t = & \epsilon A - 3|A|^2 A - (2k_0)^2 (i\partial_x + \nu)^2 A + \delta_{n,2} \frac{|\epsilon|\gamma_2}{2} A^* \\ & + (1 - \delta_{n,2}) \left( \frac{|\epsilon|^{1/2}\gamma_1}{2} \right)^2 [\eta_1 A + \delta_{n,1} d_- A^*]. \end{aligned} \quad (3.14)$$

## 3.2 Uniform and stationary solutions

In terms of the amplitude  $A$  the leading order form of the solution is

$$u \simeq A e^{i \frac{k_f}{n} x}. \quad (3.15)$$





### Chapter 3. Resonant stripe patterns

---

Constant solutions of the amplitude equation (3.14) represent  $n : 1$  wavenumber-locked, or resonant, stationary stripe patterns. To find these solutions we consider the cases  $n \neq 2$  and  $n = 2$  separately.

#### Case $n \neq 2$

For  $n \neq 2$  Equation (3.14) becomes

$$A_t = \epsilon A - 3|A|^2 A - [2k_0(i\partial_x + \nu)]^2 A + \left(\frac{\gamma}{2}\right)^2 [\eta_1 A + \delta_{n,1} d_- A^*], \quad (3.16)$$

where  $\gamma = |\epsilon|^{1/2} \gamma_1$ , and solutions are of the form

$$A = \rho_n e^{i\phi}, \quad \rho_n = \sqrt{\frac{\epsilon - (2k_0\nu)^2 + (\eta_1 + \delta_{n,1} d_-) \frac{\gamma^2}{4}}{3}}, \quad (3.17)$$

with  $\nu = k_0 - k_f/n$ . The phase  $\phi$  is constant with  $\phi = \{0, \pi\}$  for  $n = 1$  but undetermined for higher resonances for the order  $|\epsilon|^{3/2}$  of our calculation. The resonant stripe solutions exist for

$$\gamma > 2\sqrt{\frac{(2k_0\nu)^2 - \epsilon}{\eta_1 + \delta_{n,1} d_-}}. \quad (3.18)$$

#### Case $n = 2$

For  $n = 2$  Equation (3.14) becomes

$$A_t = \epsilon A - 3|A|^2 A - [2k_0(i\partial_x + \nu)]^2 A + \frac{\gamma}{2} A^*, \quad (3.19)$$

where  $\gamma = |\epsilon| \gamma_2$ , and the solutions are of the form

$$A = \rho_2 e^{i\phi}, \quad \rho_2 = \sqrt{\frac{\epsilon - (2k_0\nu)^2 + \gamma/2}{3}}, \quad (3.20)$$



with  $\phi = \{0, \pi\}$  [49]. These solutions exist for

$$\gamma > 2 \left[ (2k_0\nu)^2 - \epsilon \right] . \quad (3.21)$$

Figure 3.1 shows the tongue-shaped existence ranges of  $n:1$  resonant stripe patterns with  $n = 1, \dots, 4$ , for parameters above,  $\epsilon > 0$ , and below,  $\epsilon < 0$ , the pattern forming instability. The solid lines in the figure are the results of the analysis from Equations (3.17) and (3.20) and the shaded regions are numerical results from solving for stationary solutions of the forced SH equation (3.1) using the continuation method AUTO [73].

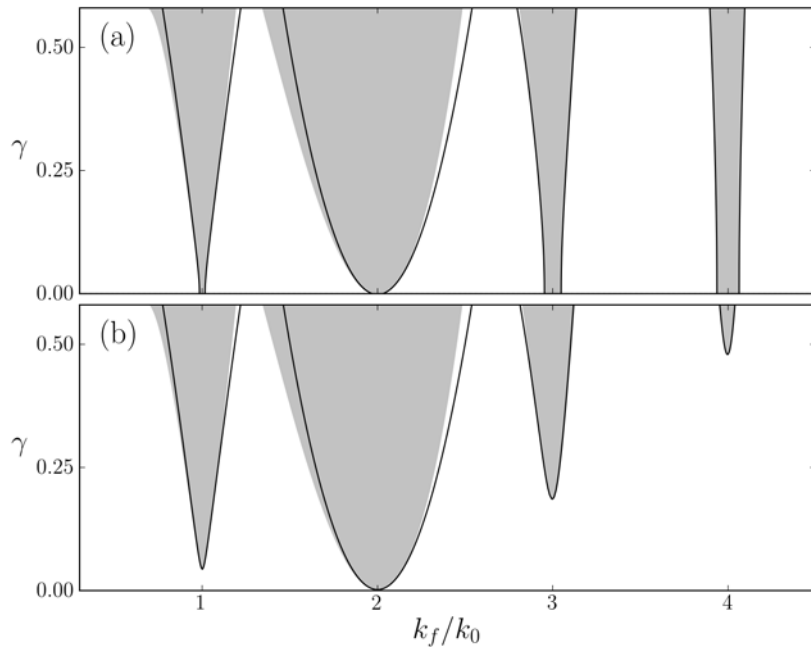
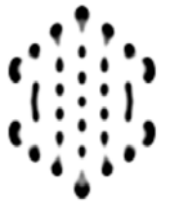


Figure 3.1: Existence domains of resonant stripe solutions of Equation (3.1), (a) above ( $\epsilon > 0$ ), and (b) below ( $\epsilon < 0$ ) the pattern forming instability. The shaded regions indicate the range of resonant solutions computed from stationary solutions of Equation (3.1), and the solid curves show the region boundary approximations (Equations. (3.18) and (3.21)) based on the amplitude equation approach. The agreement for the lower resonances is very good for sufficiently small  $\gamma$  values, and for the higher resonances it remains surprisingly good, even for large  $\gamma$  values. Parameters:  $k_0 = 1$  and (a)  $\epsilon = 0.001$ , (b)  $\epsilon = -0.001$ .



Note that for  $\epsilon > 0$  the tongues have finite width even at  $\gamma = 0$  (Figure 3.1a). This width corresponds to the band of stripe solutions of the unforced system that appears beyond the pattern-forming instability. The effect of a weak forcing with a detuning  $\nu$  can be interpreted as follows. If the detuning is small enough, the forcing selects the stripe solution within the band that resonates with  $k_f/n$ . If the detuning lies outside the band, the system can still yield to the forcing by changing the stripes wavenumber so as to resonate with  $k_f/n$ . This behavior is analogous to the frequency adjustment that a periodically forced oscillator makes when it locks to a fraction of the forcing frequency. Note also that for  $\epsilon < 0$ , i.e., below the pattern-forming instability, resonant stripe solutions are still possible, provided the forcing is strong enough (Figure 3.1b). The minimum forcing strength can be evaluated from Equations (3.18) and (3.21), e.g., the smallest  $\gamma$  value that enables locking for the 2 : 1 resonance is  $-2\epsilon$ . The forcing has the additional effect of increasing the amplitude of the stripe pattern. This effect, however, becomes diminishingly small as the forcing wavenumber increases.

The 2 : 1 resonance tongue stands out in being wider and, for  $\epsilon < 0$ , in extending to lower forcing strength  $\gamma$ . The distinct character of the 2 : 1 resonance is already seen in the amplitude equation (3.19) for the 2 : 1 resonance, as compared with the amplitude equations (3.16) for all other resonances. In the former, the forcing strength appears to linear order, whereas in the latter it only appears at the second quadratic order, and therefore has a weaker effect. The different forms of amplitude equations with respect to the forcing follow from the type of parametric forcing; forcing the cubic term in the forced SH equation (3.1), rather than the linear term, will result in a prominent 4 : 1 resonance.

Figure 3.2 shows typical examples of  $n : 1$  resonant solutions. Note that for every period of the response  $u$ , there are  $n$  periods of the forcing, which characterizes the  $n : 1$  solution.

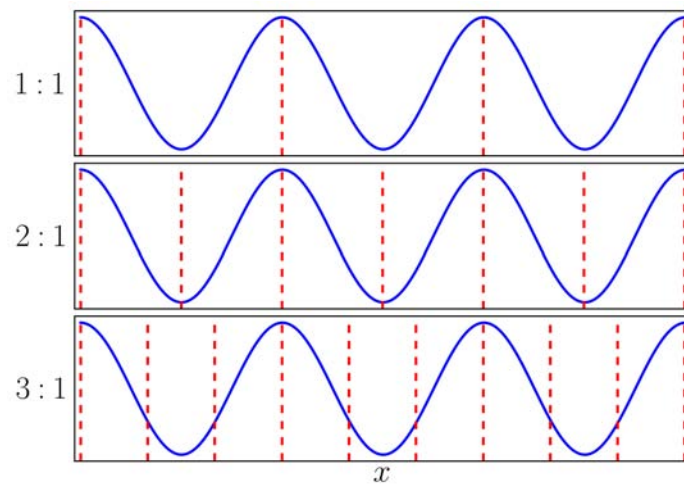
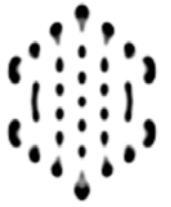


Figure 3.2: Typical  $n : 1$  wavenumber locked solutions, with  $n = 1, 2, 3$ . The continuous blue line denotes the response  $u$  of the system, and the red dashed lines denote the positions in  $x$  where the forcing  $\gamma \cos(k_f x)$  reaches its maximum.



## Chapter 4

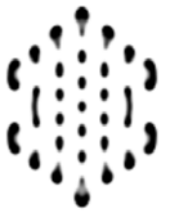
# Interference of 2d patterns

*“The most exciting phrase to hear in science, the one that heralds new discoveries, is not ‘Eureka!’ (I found it!) but ‘That’s funny...’”*

– Isaac Asimov

In 2d domains, the solutions to Equations (2.8) may respond differently to the periodic forcing from that seen in Chapter 3. In 2d the 2:1 resonance is much more dominant and even a purely 1d forcing,  $\mathbf{k}_f = k_f \hat{x}$ , can induce stable 2d patterns [49] — oblique patterns for  $\gamma < \epsilon$  and rectangular patterns for  $\gamma > \epsilon$ , as we saw in the Background chapter. These are resonant patterns that respond to the spatial forcing by locking the wavevector components in the forcing direction in 2:1 resonance,  $k_x = k_f/2$ , and creating a wavevector component in the orthogonal direction,  $k_y$ , to compensate for the unfavorable forcing wavenumber, so that  $k_x^2 + k_y^2 = k_0^2$ .

The range of existence of these 2d patterns is very wide in the forcing wavenumber  $k_f$ . It extends all the way to  $k_f = 0$  and is bounded from above at  $k_f = 2k_0$ , the point where the component  $k_x$  attains its maximal possible value,  $k_0$ . As shown in Figure 4.1, this range of 2d patterns overlaps the resonance tongue of 1d patterns described earlier and both patterns can exist at the same parameter values. The continuous black curves demarcate regions of existence of 1d stripe solutions, and the green and blue shaded areas mark the regions where rectangular and oblique patterns are found,



respectively. Figure 4.2 shows typical examples of 1 : 1 stripe patterns and of 2d rectangular patterns, both for the same point in the parameter space. Depending on initial conditions, one can take the system to respond very differently to the 1d forcing, as indicated by the Fourier spectra of both solutions.

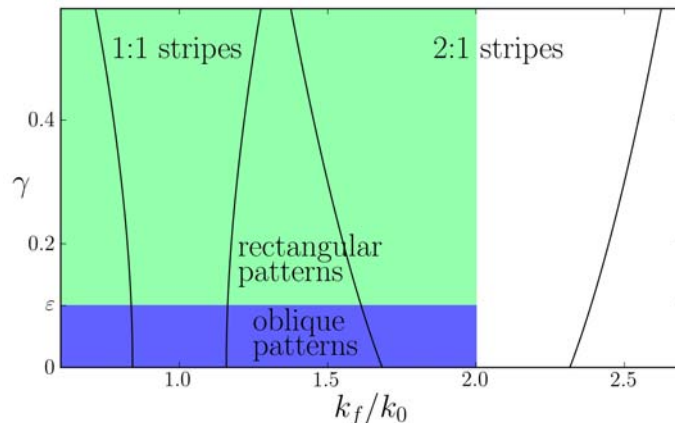


Figure 4.1: The existence domains of resonant rectangular and oblique patterns are very wide and overlap with the resonance tongues of 1 : 1 and 2 : 1 stripe patterns. Parameters:  $\epsilon = 0.1$ .

Which patterns persist in the overlap region of rectangular and oblique patterns with the 1 : 1 resonance tongue of stripe patterns? In order to study the interaction of the patterns, we approximate solutions of Equation (2.8) as a superposition of a stripe mode with amplitude  $A$  and two oblique modes with amplitudes  $a$  and  $b$ ,

$$u \simeq A e^{ik_0 x} + a e^{i(k_x x + k_y y)} + b e^{i(k_x x - k_y y)} + C.C., \quad (4.1)$$

where  $k_x = k_f/2$  is the  $\hat{x}$  component of the oblique wavevectors, and it is chosen to represent a 2 : 1 resonance, and  $k_y$  is the  $\hat{y}$  component. The amplitudes  $A$ ,  $a$ , and  $b$  vary weakly in time and space. The variable  $u$  and the time and space derivatives were all naively expanded in a  $|\epsilon|^{i/4}$  power series in order to guarantee that all terms in the amplitude equations are mutually balanced. A detailed multiple time-scale analysis of the stripe and oblique modes can be found below.

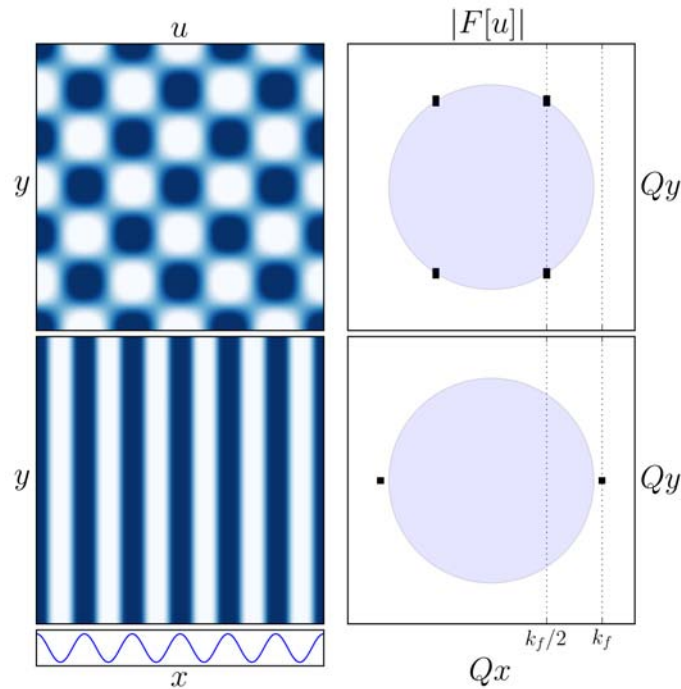
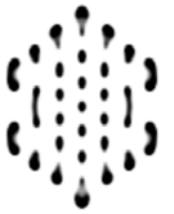


Figure 4.2: Two stable solutions of Equation (2.8), for the same parameter values. The panel on the upper left side shows a 2 : 1 locked rectangular solution, and the panel below it shows a 1 : 1 locked stripe solution. The short panel on the lower left side shows the forcing  $\gamma \cos(k_f x)$ . The panels on the right show the Fourier transform of the respective solutions, and the circle in light blue has radius  $k_0$ . Parameters:  $\epsilon = 0.1$ ,  $\gamma = 0.2$  and  $k_f = 1.08$ .

## 4.1 Multiple scales analysis

### 4.1.1 Scaling

We study the interaction between stripes and rectangular or oblique patterns by deriving equations for the amplitudes of a stripe mode and of two oblique modes using the leading order approximation

$$u \simeq A e^{ik_0 x} + a e^{i(k_x x + k_y y)} + b e^{i(k_x x - k_y y)} + C.C., \quad (4.2)$$



## Chapter 4. Interference of 2d patterns

---

for the solutions of Equation (2.8), where the amplitudes are assumed to vary slowly in space and time. Specifically, we define the slow variables

$$x_i = \epsilon^{i/4} x, \quad y_i = \epsilon^{i/4} y, \quad t_i = \epsilon^{i/4} t, \quad i = 1, 2, \dots, \quad (4.3)$$

and assume the following amplitude dependence:

$$\begin{aligned} A &= A(y_1, x_2, y_2, t_1, t_2, \dots), \\ a &= a(x_2, y_2, t_1, t_2, \dots), \quad b = b(x_2, y_2, t_1, t_2, \dots). \end{aligned} \quad (4.4)$$

We included a dependence of  $A$  on  $y_1$  in order to capture a possible zigzag instability of stripe solutions. We further assume the following scaling forms for the forcing parameters:

$$\gamma = |\epsilon|^{1/2} \gamma_1, \quad \nu = |\epsilon|^{1/2} \nu_1, \quad (4.5)$$

where  $\gamma_1$  and  $\nu_1$  are of order unity.

In deriving the amplitude equation (3.16) for stripes in the previous chapter, we used the scaling  $\gamma \sim |\epsilon|^{1/2}$ , whereas in the derivation of the amplitude equations for the two oblique modes in Chapter 2, the scaling  $\gamma \sim |\epsilon|$  has been used. Because we are interested in deriving coupled equations for stripe and oblique modes we need to use the same scaling for  $\gamma$ . Choosing  $\gamma \sim |\epsilon|^{1/2}$  and slow time scales  $t_i = \epsilon^{i/2} t$ , as in Ref. [74], leads to the undesired result that the forcing terms in the amplitude equations for the oblique modes are the largest with no other terms of the same order of magnitude to balance them. We therefore choose the slow time scales as in (4.3) and expand the solution in powers of  $|\epsilon|^{1/4}$ :

$$u = \sum_{i=1}^{\infty} \epsilon^{i/4} u_i. \quad (4.6)$$





### 4.1.2 Order $|\epsilon|^{1/4}$

Substituting Equations (4.3), (4.5) and (4.6) into Equation (2.8) we find at order  $|\epsilon|^{1/4}$

$$\mathcal{L}^2 u_1 = 0, \quad (4.7)$$

where  $\mathcal{L} = \mathcal{M}_{00} + k_0^2$  and  $\mathcal{M}_{ij} = \partial_{x_i} \partial_{x_j} + \partial_{y_i} \partial_{y_j}$ . Equation (4.7) has a solution of the form

$$u_1 = A e^{ik_0 x_0} + a e^{i(k_x x_0 + k_y y_0)} + b e^{i(k_x x_0 - k_y y_0)} + C.C., \quad (4.8)$$

where  $k_x^2 + k_y^2 = k_0^2$ , which justifies the leading order approximation (4.2).

### 4.1.3 Order $|\epsilon|^{2/4}$

At order  $|\epsilon|^{2/4}$  we find

$$\mathcal{L}^2 u_2 = -\partial_{t_1} u_1 + \mathcal{L} \mathcal{M}_{01} u_1. \quad (4.9)$$

Note that the term  $\mathcal{L} \mathcal{M}_{01} u_1$  that appears on the right side of Equation (4.9) equals to zero because the operators  $\mathcal{L}$  and  $\mathcal{M}_{ij}$  commute and  $\mathcal{L} u_1 = 0$ . Therefore, from now on we will omit terms of the kind  $\mathcal{L} \mathcal{M}_{ij} u_1$  from the analysis. Applying the solvability condition to secular terms on the right-hand side of Equation (4.9) we find that neither mode depends on  $t_1$ ,

$$\partial_{t_1} A = 0, \quad \partial_{t_1} a = 0, \quad \partial_{t_1} b = 0. \quad (4.10)$$

Hence,  $u_2$  satisfies the same equation as  $u_1$  and we can choose the trivial zero solution,  $u_2 = 0$ .

### 4.1.4 Order $|\epsilon|^{3/4}$

At order  $|\epsilon|^{3/4}$  we have

$$\mathcal{L}^2 u_3 = -\partial_{t_2} u_1 - 4\mathcal{M}_{01}^2 u_1 - u_1^3 + u_1 \gamma_1 \cos(k_f x_0). \quad (4.11)$$



We recall that we focus on the overlap range of the 1 : 1 resonance tongue, where  $k_f = k_0 - \nu = k_0 - |\epsilon|^{1/2} \nu_1$ , with 2:1 resonant rectangular or oblique patterns for which  $k_f = 2k_x$ . Substituting Equation (4.8) into Equation (4.11), and demanding solvability, we find

$$\begin{aligned}\partial_{t_2} A &= F(A), \\ \partial_{t_2} a &= F(a) + \frac{\gamma_1}{2} b^*, \\ \partial_{t_2} b &= F(b) + \frac{\gamma_1}{2} a^*,\end{aligned}\tag{4.12}$$

where  $F(\zeta) = -3(2|A|^2 + 2|a|^2 + 2|b|^2 - |\zeta|^2)\zeta$ . If we were to stop the analysis here, the amplitude equation for the stripe pattern would not include any forcing term. Therefore, we continue the analysis to higher orders in  $|\epsilon|$  until a forcing term is achieved for the stripe equation. We will simplify the calculations from this point on by using the following symmetry argument. Since the forced SH equation is invariant under the reflection symmetry  $y \rightarrow -y$ ,  $u(x, -y)$  must also be a solution. The solution form Equation (4.2) then implies that  $b$  should satisfy the same amplitude equation as  $a$  once  $a$  and  $b$  are exchanged and  $y$  is replaced by  $-y$ . Thus from now on we do not present the solvability conditions associated with  $b$ .

A particular solution to Equation (4.11) is given by

$$\begin{aligned}u_3 = & -\frac{1}{64k_0^4} (E_1^3 + E_2^3 + E_3^3) - 3d_2 (E_2 + E_3) E_2 E_3 \\ & - 3p_+ [E_1 (E_2^2 + E_3^2) + E_1^2 (E_2 + E_3)] - 6d_+ E_1 E_2 E_3 \\ & - 3p_- [E_1^* (E_2^2 + E_3^2) + E_1^{*2} (E_2^* + E_3^*)] - 6d_- E_1^* E_2 E_3 \\ & - 3d_1 [(E_3^* E_2^2 + E_2^* E_3^2) + 8(E_2 E_3^* + E_2^* E_3) E_1] \\ & + \frac{\gamma_1}{2} e^{ik_f x_0} [d_+ E_1 + d_2 (E_2 + E_3) + d_- E_1^*] + C.C.,\end{aligned}\tag{4.13}$$

where  $E_1 = A e^{ik_0 x_0}$ ,  $E_2 = a e^{i(k_x x_0 + k_y y_0)}$ ,  $E_3 = b e^{i(k_x x_0 - k_y y_0)}$ , and the coefficients are

$$d_{\pm} = \frac{1}{k_f^2 (k_f \pm 2k_0)^2}, \quad d_1 = \frac{1}{64k_y^4}, \quad d_2 = \frac{1}{4k_f^4}, \quad p_{\pm} = \frac{k_f^2}{4k_0^2} d_{\pm}.\tag{4.14}$$



#### 4.1.5 Order $|\epsilon|^{4/4}$

At order  $|\epsilon|^{4/4}$  we obtain

$$\mathcal{L}^2 u_4 = -\partial_{t_3} u_1 - 4\mathcal{M}_{01} [(\mathcal{M}_{11} + 2\mathcal{M}_{02}) u_1 + \mathcal{L} u_3]. \quad (4.15)$$

Requiring solvability we find that neither mode depends on  $t_3$ :

$$\partial_{t_3} A = 0, \quad \partial_{t_3} a = 0, \quad \partial_{t_3} b = 0. \quad (4.16)$$

There is no need to solve Equation (4.15) explicitly, because in the next and last order we consider the term that contains  $u_4$ ,  $(\mathcal{L}\mathcal{M}_{01}u_4)$  is not secular and will not contribute to the amplitude equations up to the order  $|\epsilon|^{5/4}$  considered here.

#### 4.1.6 Order $|\epsilon|^{5/4}$

The final order  $|\epsilon|^{5/4}$  gives

$$\begin{aligned} \mathcal{L}^2 u_5 = & -\partial_{t_4} u_1 - \partial_{t_2} u_3 - 4\mathcal{L}\mathcal{M}_{01}u_4 - 2[2\mathcal{M}_{01}^2 + \mathcal{L}(2\mathcal{M}_{02} + \mathcal{M}_{11})]u_3 \\ & - [(2\mathcal{M}_{02} + \mathcal{M}_{11})^2 + 8\mathcal{M}_{01}\mathcal{M}_{12}]u_1 - 3u_1^2 u_3 + u_1 + \gamma_1 u_3 \cos k_f x_0. \end{aligned} \quad (4.17)$$

Applying the solvability condition, we find

$$\begin{aligned} \partial_{t_4} A = & A + G + (2k_0 \partial_{x_2} - i\partial_{y_1}^2)^2 A + 3\gamma_1 \eta_1 \left( \frac{\gamma_1}{12} - ab - a^* b^* \right) A \\ & + e^{-2i\nu_1 x_2} \left( \frac{d_- \gamma_1 a^2}{4} - \frac{\gamma_1}{2} ab \eta_2 + 6a^2 b^2 \eta_4 \right) A^*, \\ \partial_{t_4} a = & a + H(a, b) + 4(k_x \partial_{x_2} + k_y \partial_{y_2})^2 a + \frac{3\gamma_1 d_2}{2} \left( \frac{\gamma_1}{6} - ab \right) a \\ & + \left[ -3\gamma_1 \left( |a|^2 d_2 + |b|^2 \frac{d_2}{2} + |A|^2 \eta_1 \right) + e^{2i\nu_1 x_2} \left( -\frac{\gamma_1}{2} \eta_3 + 3a^* b^* \eta_5 \right) A^2 \right] b^*, \end{aligned} \quad (4.18)$$



where

$$\begin{aligned}\eta_1 &= d_+ + d_-, & \eta_2 &= 12(d_2 + d_-), & \eta_4 &= 3d_2 + \eta_3, \\ \eta_3 &= 3d_2 + 3p_- + 6d_-, & \eta_5 &= 3d_2 + 15p_- + 12d_-, \end{aligned} \quad (4.19)$$

and

$$\begin{aligned}G &= 3 \left[ \frac{|A|^4}{64k_0^4} + 3(p_+ + p_-) (2|A|^2|a|^2 + 2|A|^2|b|^2 + |a|^4 + |b|^4) \right. \\ &\quad \left. + 12(\eta_1 + 8d_1)|a|^2|b|^2 \right] A, \\ H(\zeta_1, \zeta_2) &= 3 \left[ \frac{|\zeta_1|^4}{64k_0^4} + 3|A|^2(|A|^2 + 2|\zeta_1|^2)(p_+ + p_-) \right. \\ &\quad \left. + 3|\zeta_2|^2(2|\zeta_1|^2 + |\zeta_2|^2)(d_1 + d_2) + 12|A|^2|\zeta_2|^2(\eta_1 + 8d_1) \right] \zeta_1. \end{aligned} \quad (4.20)$$

### 4.1.7 Amplitude equations

The amplitude equations can now be obtained by combining Equations (4.10), (4.12), (4.16) and (4.18) (using the chain rule). Rescaling back to the “fast” space and time variables and rescaling the amplitudes  $A \rightarrow \epsilon^{-1/4} e^{-i\nu_1 x_2} A$ ,  $a \rightarrow \epsilon^{-1/4} a$ ,  $b \rightarrow \epsilon^{-1/4} b$ , the detuning  $\nu_1 = \epsilon^{-1/2} \nu$  and the forcing strength as  $\gamma_1 = \epsilon^{-1/2} \gamma$ , gives the final form of the amplitude equations (we have also added the symmetric equation for  $b$ ),

$$\begin{aligned}\partial_t A &= \epsilon A - 3(|A|^2 + 2|a|^2 + 2|b|^2) A - [2k_0(i\partial_x + \nu) + \partial_y^2]^2 A \\ &\quad + \left(\frac{\gamma}{2}\right)^2 (\eta_1 A + d_- A^*) + \hat{G}, \\ \partial_t a &= \epsilon a - 3(|a|^2 + 2|b|^2 + 2|A|^2) a + 4(k_x \partial_x + k_y \partial_y)^2 a \\ &\quad + \frac{\gamma}{2} b^* + \hat{H}(a, b), \\ \partial_t b &= \epsilon b - 3(|b|^2 + 2|a|^2 + 2|A|^2) b + 4(k_x \partial_x - k_y \partial_y)^2 b \\ &\quad + \frac{\gamma}{2} a^* + \hat{H}(b, a), \end{aligned} \quad (4.21)$$



with

$$\begin{aligned}
 \hat{G} &= -3\gamma\eta_1 (ab + a^*b^*) A + \left[ -\frac{\gamma}{2}ab\eta_2 + 6a^2b^2\eta_4 \right] A^* + G, \\
 \hat{H}(a, b) &= \frac{3\gamma d_2}{2} \left( \frac{\gamma}{6} - ab \right) a + \left( -\frac{\gamma}{2}\eta_3 + 3a^*b^*\eta_5 \right) A^2b^* \\
 &\quad - 3\gamma \left[ |a|^2 d_2 + |b|^2 \frac{d_2}{2} + |A|^2 \eta_1 \right] b^* + H(a, b).
 \end{aligned} \tag{4.22}$$

In the derivation of Equations (4.21) we have considered particular solutions of the equations for  $u_i$  instead of general solutions with free fields for the different modes. In principle, these fields can be determined by demanding commutativity between time derivatives for each mode, e.g.  $\partial_{t_4}(\partial_{t_2}A) = \partial_{t_2}(\partial_{t_4}A)$  [75]. Implementing these conditions, however, turned out to be too hard. Nevertheless, the amplitude equations (4.21) capture the essential physics, and provide good quantitative approximations, at least for sufficiently small  $\gamma$ , as Figure 4.3 indicates.

We note that Equations (4.21) reduce to known equations for either stripe patterns or 2d patterns when the appropriate limits are considered. For stripe solutions  $(A, 0, 0)$  they coincide with Equation (3.14) when  $n = 1$  and disregarding  $\hat{G}$ , which contains higher (fifth) order contributions. For rectangular and oblique solutions they reduce to the Equations (2.22) derived in Chapter 2 when disregarding the fifth order contributions in  $\hat{H}$ .

The analysis is taken up to order  $|\epsilon|^{5/4}$ , which is necessary to yield space derivatives in  $y$  and quintic terms in  $A$  and  $A^*$ . When these terms are neglected and the amplitudes  $a = b = 0$ , the amplitude equations (4.21) reduce to Equation (3.16) for the case  $n = 1$ .

## 4.2 Uniform and stationary solutions

Constant solutions of the amplitude equations (4.21) of the form  $(A, 0, 0)$  represent 1 : 1 stripe patterns, while constant solutions of the form  $(0, a, b)$  represent rectangular or oblique patterns locked in a 2 : 1 resonance in the  $\hat{x}$



direction. The resonant stripe solutions are given by

$$A_s = \rho_{s\pm} e^{i\phi_s}, \quad (4.23)$$

where

$$\rho_{s\pm} = 2\sqrt{8k_0^4 \pm (k_0^2/\sqrt{3})\sqrt{\epsilon_s}}, \quad \phi_s = m\frac{\pi}{2}. \quad (4.24)$$

Here

$$\epsilon_s = -4\epsilon + 16k_0^2(\nu^2 + 12k_0^2) - \gamma_1^2\{d_+ + [(-1)^m + 1]d_-\}, \quad (4.25)$$

and  $m$  is an integer. For even (odd) values of  $m$ , the solution  $\phi_s$  is stable (unstable).

Resonant rectangular solutions are given by

$$a = \rho_r e^{i\phi_a}, \quad b = \rho_r e^{i\phi_b}, \quad (4.26)$$

where

$$\rho_{r\pm} = \sqrt{\frac{9 \pm \sqrt{81 - 4c\epsilon_r}}{2c}}, \quad \phi_a + \phi_b = m\pi. \quad (4.27)$$

Here

$$\epsilon_r = \epsilon + (-1)^m \frac{\gamma_2}{2}, \quad c = \frac{27}{4} (k_f^{-4} + (k_f^2 - 4)^{-2}), \quad (4.28)$$

and we assumed weak forcing strength ( $\gamma_1 = 0$ ). For even (odd) values of  $m$ , the solutions  $\phi_a, \phi_b$  are stable (unstable).

Because all solutions with odd values of  $m$  are unstable, we will restrict our further consideration to even  $m$  only.

### 4.3 Stability analysis of stripe patterns

To see how the 2d resonant patterns affect the stability of the 1 : 1 resonant stripes we analyze the stability of the solutions  $(A, a, b) = (\pm\rho_{s\pm}, 0, 0)$ . We introduce nonuniform perturbations in the following way:



$$\begin{pmatrix} A \\ a \\ b \end{pmatrix} = \begin{pmatrix} A_0 \\ 0 \\ 0 \end{pmatrix} + \Delta \begin{pmatrix} \delta A_+ \\ \delta a_+ \\ \delta b_+ \end{pmatrix} e^{i(q_x x + q_y y)} + \Delta \begin{pmatrix} \delta A_-^* \\ \delta a_-^* \\ \delta b_-^* \end{pmatrix} e^{-i(q_x x + q_y y)}. \quad (4.29)$$

Substituting Equation (4.29) into the amplitude equations (4.21), and keeping only linear terms in  $\Delta$ , we have the following  $6 \times 6$  Jacobian matrix:

$$J = \begin{pmatrix} J_1 & 0 \\ 0 & J_2 \end{pmatrix}, \quad (4.30)$$

where

$$J_1 = \begin{pmatrix} J_1^- & J_1^0 \\ J_1^0 & J_1^+ \end{pmatrix}, \quad J_2 = \begin{pmatrix} J_2^+ & 0 & 0 & J_2^0 \\ 0 & J_2^+ & (J_2^0)^* & 0 \\ 0 & J_2^0 & J_2^- & 0 \\ (J_2^0)^* & 0 & 0 & J_2^- \end{pmatrix}, \quad (4.31)$$

and

$$\begin{aligned} J_1^\pm &= \epsilon - 6|A_0|^2 + \frac{9}{64k_0^4}|A_0|^4 + \eta_1 \left(\frac{\gamma}{2}\right)^2 - q_y^4 + 4q_y^2(\nu \pm q_x)k_0 - 4(\nu \pm q_x)^2 k_0^2 \\ J_1^0 &= -3A_0^2 + \frac{3}{32k_0^4}|A_0|^2 A_0^2 + d_- \left(\frac{\gamma}{2}\right)^2 \\ J_2^\pm &= \epsilon - 6|A_0|^2 + 9(p_+ + p_-)|A_0|^4 + d_2 \left(\frac{\gamma}{2}\right)^2 - 4(k_x q_x \pm k_y q_y)^2 \\ J_2^0 &= -\frac{1}{2}\gamma(6\eta_1|A_0|^2 + \eta_3 A_0^2 - 1). \end{aligned} \quad (4.32)$$

The Jacobian matrix  $J$  has a block diagonal form, with one block representing the stripe mode and the other block representing the oblique modes. Accordingly, one pair of eigenvalues,  $\sigma_{s\pm}$ , describes the dynamics of perturbations along the stripe mode, and another eigenvalue pair of multiplicity two,  $\sigma_{r\pm}$ , describes the dynamics of perturbations along the oblique modes.



Of these only the eigenvalues  $\sigma_{s+}$  and  $\sigma_{r+}$  are potentially positive or have positive real parts.

For the stripe solutions  $A_0 = \pm\rho_{s+}$ , both  $\sigma_{s+}$  and  $\sigma_{r+}$  are positive in the whole parameter range studied, and thus these solutions are always unstable, and will not be considered any further. For the stripe solutions  $A_0 = \pm\rho_{s-}$ , the analysis of eigenvalue  $\sigma_{r+}$  shows that there exists a domain in the existence overlap region of 1 : 1 stripes and rectangular patterns where the resonant stripes are stable, but the size of this domain is reduced by the growth of oblique modes. Furthermore, the reduced stability domain has two distinct shapes depending on the value of  $\epsilon$ . For relatively large values,  $\epsilon > \epsilon_c \simeq 0.036$  (with  $k_0 = 1$ ), there is a continuous  $\gamma$  range in which stripe solutions are stable, while for  $\epsilon < \epsilon_c$ , the stability range is split into two regions, as Figure 4.3 shows. The light-gray shades show the existence range of stripe solutions,  $A = \pm\rho_{s-}$ , while the dark-gray shades show their stability ranges (where both  $\sigma_{s+}$  and  $\sigma_{r+}$  are negative), for (a)  $\epsilon > \epsilon_c$  and (b)  $\epsilon < \epsilon_c$ .

The surprising result is that for  $\epsilon < \epsilon_c$  there is an intermediate range of forcing strength  $\gamma$  where the forcing destabilizes the stripe patterns even at exact resonance  $k_f = k_0$ . In the 1d system studied before, the forcing always acted to stabilize the stripe patterns, but in 2d it induces the growth of rectangular and oblique patterns, which may restrict the stability region of the 1 : 1 resonant stripes.

The asymmetry in the stability region for low  $\gamma$  values is due to two different kinds of instabilities related to the eigenvalue  $\sigma_{s+}$ . In the lower part of Figure 4.3 (for values of  $\gamma$  between 0 and approximately 0.1), the left border of the stable stripes region (dark gray) indicates a zigzag instability, associated with the growth of perturbations of the form  $e^{q_y y}$ . On the border on the right side, for very low values of  $\gamma$  (between 0 and approximately 0.02), an Eckhaus instability, associated with the growth of perturbations of the form  $e^{iq_x x}$ , occurs. These results are qualitatively similar to the effects of the zigzag and Eckhaus instabilities found in the 2 : 1 resonance of stripe patterns [49].

Numerical solutions of Equation (2.8) confirm the predictions of the mathematical analysis. The hollow circles in Figure 4.3 show the borders of the



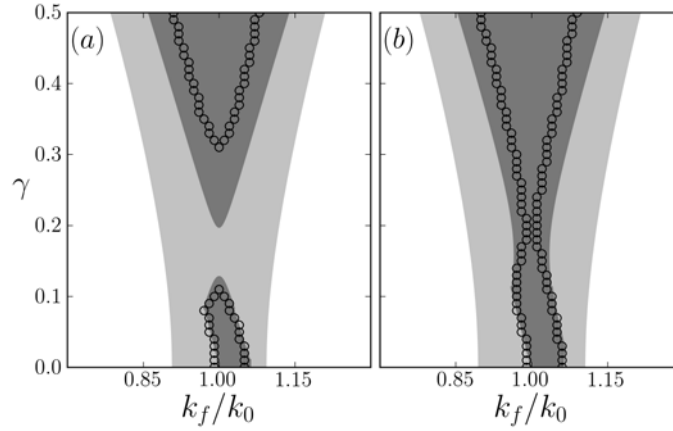


Figure 4.3: Existence and stability domains of 1:1 resonant stripe solutions of Equations (4.21). The light gray shaded areas indicate the existence domains and the dark gray shaded areas are the stability regions. (a) Above the critical value,  $\epsilon > \epsilon_c$ , the stable region is contiguous. (b) Below the critical point,  $\epsilon < \epsilon_c$  the solution is not stable in a range of forcing amplitude  $\gamma$  even at exact resonance  $k_f = k_0$ . Parameters: (a)  $\epsilon = 0.035$ , (b)  $\epsilon = 0.045$ .

stability region, and the agreement between simulation and analysis is very good for low values of  $\gamma$ . Because of the choice of weak forcing strength ( $\gamma_1 = 0$ ), the analysis is expected to better describe the simulations for small values of  $\gamma$ , in line with the results shown in Figure 4.3. The numerical integration performed was the explicit Euler method to advance time, and a semi-spectral method to calculate the space derivatives (see Appendix), with a 1 : 1 stripe pattern as initial condition, with a small random noise added to it. The critical value we found was  $\epsilon_c \simeq 0.043$ , about 15% from our theoretically calculated value of  $\epsilon = 0.036$ .

## 4.4 Functional competition

The stability regions of the 1 : 1 stripe solution in Figure 4.3, as well as the stability regions of the 2 : 1 stripe solution [48, 49], are actually *bistability* regions of the stripe patterns and 2d patterns. This raises the question of which pattern is dominant, i.e., which pattern invades the other in these ranges. To study this question, we calculated the energy (Lyapunov) functional of



Equation (2.8):

$$F = \int d\mathbf{r} \left( -\frac{1}{2}[\epsilon + \gamma \cos(k_f x)]u^2 + \frac{1}{4}u^4 + \frac{1}{2}(\nabla^2 u + k_0^2 u)^2 \right). \quad (4.33)$$

Because the system is variational, when two bistable solutions are mixed, the one with lowest energy is dominant, and will invade the other. Figure 4.4 shows the energies of rectangular patterns, resonant 1 : 1 stripe patterns, and resonant 2 : 1 stripe patterns, calculated from their respective analytical forms. The energy of each solution is shown in its existence range along the  $k_f/k_0$  axis. The energy of the 1 : 1 stripe pattern is higher than that of the rectangular pattern, implying that the latter is dominant. This is supported by numerical integrations of Equation (2.8), according to which the rectangular patterns invade the 1:1 stripe, as the snapshots in Figure 4.5a show. This result holds even at exact resonance ( $k_f = k_0$ ). The situation is different within the resonance range of 2 : 1 stripes; the energies of the stripe and rectangular patterns cross one another and split the range into a low- $k_f$  part, where the rectangular patterns are dominant and a high- $k_f$  part, where the stripe pattern is dominant. Indeed, numerical integrations of Equation (2.8) show that in the low- $k_f$  part the rectangular pattern invades the stripe pattern (Figure 4.5b) and in the high- $k_f$  part the stripe pattern invades the rectangular pattern (Figure 4.5c).

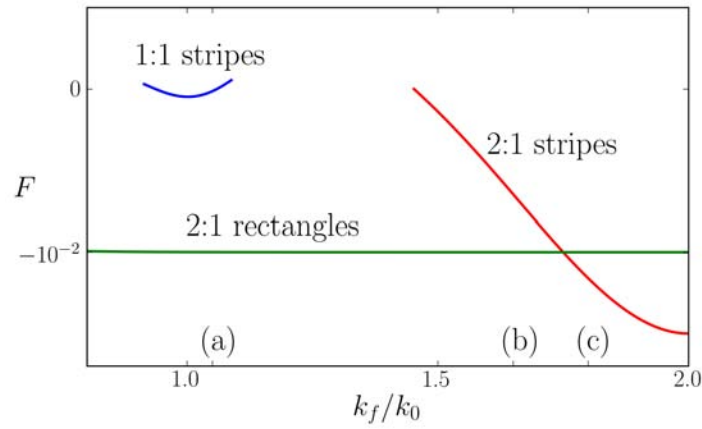


Figure 4.4: The energy (Lyapunov functional values) of 1 : 1 resonant stripe patterns, 2:1 resonant stripe patterns, and rectangular patterns. Parameters:  $\epsilon = 0.1$ ,  $\gamma = 0.4$ .

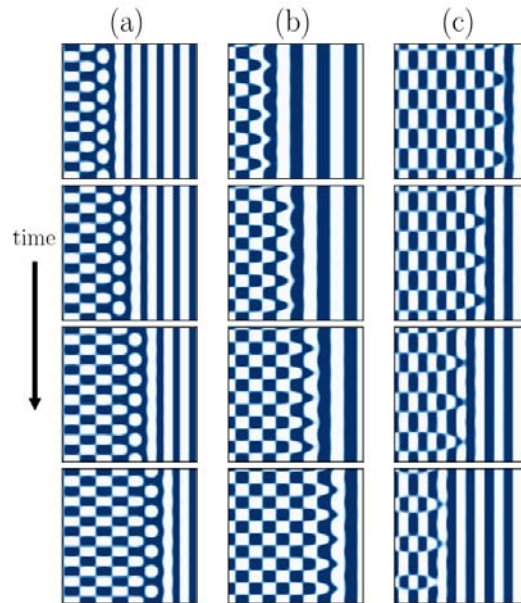


Figure 4.5: Snapshots of the dynamics of fronts that separate stripe and rectangular patterns. Lower energy patterns invade the regions of higher energy patterns: (a) rectangular pattern invading 1:1 stripes ( $k_f/k_0 = 1.10$ ), (b) rectangular pattern invading 2 : 1 stripes ( $k_f/k_0 = 1.65$ ), and (c) 2 : 1 stripes invading a rectangular pattern ( $k_f/k_0 = 1.80$ ). The domain sizes of simulations (a), (b) and (c) are  $50 \times 50$ ,  $60 \times 60$  and  $50 \times 50$ , respectively. Parameters:  $\epsilon = 0.1$ ,  $\gamma = 0.4$ .



## Chapter 5

# Vegetation

*“In theory, there is no difference between theory and practice.  
But, in practice, there is.”*

– Jan L. A. van de Snepscheut

In recent years there has been much interest in studying the rehabilitation of damaged ecological systems [76, 77]. The first step of rehabilitation is recovery of vegetation, which can be achieved in drylands by the harvesting of runoff water in hill slopes. A common water-harvesting practice is the construction of parallel contour ditches – termed *shikim* – which accumulate runoff water from the uphill areas, and along which trees are planted [78, 79]. Controlled experiments with shikim systems have shown significant growth and survival of trees, increased pasture productivity, and increased plant diversity. In the northern Negev desert, in Israel, the shikim technique is widely used by the Jewish National Fund for reforestation of bare areas with minimal vegetation cover. Figure 5.1 shows four stages of the process, in the “Ambassadors Forest”, a few kilometers north of Beer Sheva.

An important factor in the success of rehabilitation in this kind of practice is the fact that vegetation in water limited regions can self-organize in patterns. Figure 5.2 shows four kinds of natural patterns in drylands vegetation systems, in Sudan and in Namibia, but as was pointed out in Section 2.2, these kinds of patterns can be found all over the world.

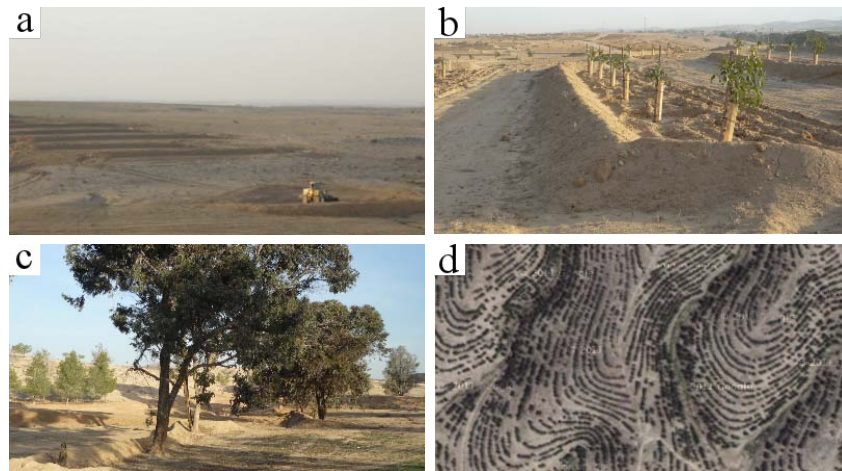
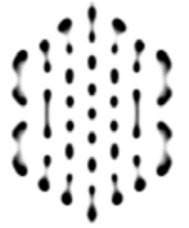


Figure 5.1: Four stages of the rehabilitation of a desert area by the shikim technique. (a) A tractor builds contour ditches along a hill slope. (b) Seedlings are planted in the shikim. (c) Mature trees along shikim. (d) Air photo of an older part of the “Ambassadors’ Forest” (picture from Google maps).

Because undisturbed natural systems in drylands can form patterns with a typical wavelength, the shikim technique can be understood as spatial periodic forcing applied to a pattern forming system. Using the same terminology as in the previous chapters, the parallel tree lines planted along the shikim constitute a  $1 : 1$  wavenumber-locked solution.

The periodic dikes built on the hill slope redistribute the runoff, which changes the spatial distribution of soil water, and thus indirectly affect the growth rate of the biomass. The biomass growth function  $G_B$  in Equation (2.26a) is a function of the soil water, and it multiplies the state variable  $B$ . For this reason, the spatial periodic forcing that the shikim produce can be understood as a parametric forcing.

In light of the results presented in Chapters 3 and 4, we can ask the following questions with regard to rehabilitation of vegetation in drylands:

- Can periodic spatial forcing be used to take a bare soil solution to a patterned solution?
- Besides  $1 : 1$  wavenumber locked solutions, are there other possible

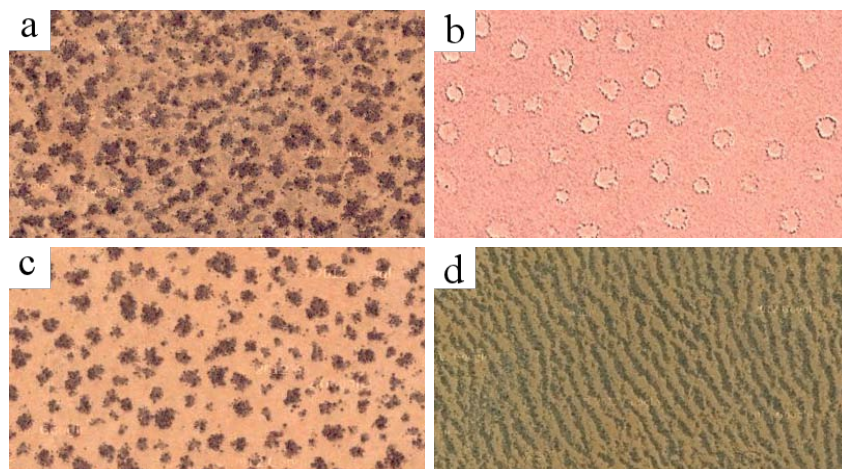


Figure 5.2: Four kinds of self-organized vegetation patterns. (a) A labyrinth pattern in Sudan, with typical length scale of 50m. Coordinates:  $11^{\circ}08'N$   $27^{\circ}50'E$ . (b) Fairy circles (holes) in Namibia, with typical length scale of 20m. Coordinates:  $25^{\circ}00'S$   $16^{\circ}00'E$ . (c) Vegetation spots in Sudan, with typical length scale of 50m. Coordinates:  $11^{\circ}37'N$   $27^{\circ}57'E$ . (d) Tiger bush (stripes) in Sudan, with typical length scale of 150m. Coordinates:  $11^{\circ}04'N$   $28^{\circ}18'E$ . Images from Google maps.

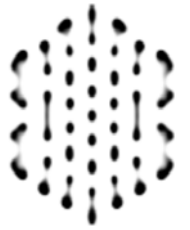
vegetation patterns, like the rectangular pattern in a  $2:1$  resonance?

- Do different patterns have different stability ranges along the precipitation rate axis? What happens when climatic changes occur, such as prolonged droughts?
- To what extent does the parametrically forced SH equation describe the general features of a vegetation system? What are the main differences and similarities?

In this chapter we will address these questions.

## 5.1 The simplified vegetation model

The vegetation model we will work with is the system introduced by Gilad et al., seen in section 2.2. The model is relatively complex for our purposes,



and we will now develop a simplification of it. Of the three water-biomass feedbacks present in the model, we leave only the infiltration feedback, which is important to account for the water harvesting role of the spatial periodic forcing. The simplification will be accomplished by changing some of the parameters of the model. Table 5.1 summarizes the parameters of the system before the simplification, with their description, units, and typical values (as they appear in [51]). To make notation simpler, we define the surface density  $\sigma = \text{kg}/\text{m}^2$ .

variable	description	units	value
$\Lambda$	biomass growth rate	$\sigma^{-1} \text{yr}^{-1}$	0.032
$E$	root augmentation per biomass unit	$\sigma^{-1}$	3.5
$S_0$	minimal root-system size	m	0.125
$K$	maximum standing biomass	$\sigma$	1
$M$	mortality rate	$\text{yr}^{-1}$	1.2
$A$	infiltration rate in fully vegetated soil	$\text{yr}^{-1}$	40
$Q$	biomass reference value	$\sigma$	0.05
$f$	infiltration contrast	1	0.1
$N$	soil water evaporation rate	$\text{yr}^{-1}$	4
$R$	evaporation reduction due to shading	1	0.95
$\Gamma$	soil water consumption rate	$\sigma^{-1} \text{yr}^{-1}$	20
$P$	precipitation rate	$\sigma$	[0,1000]
$D_B$	seed dispersal coefficient	$\text{m}^2 \text{yr}^{-1}$	$6.25 \times 10^{-4}$
$D_W$	transport coefficient for soil water	$\text{m}^2 \text{yr}^{-1}$	$6.25 \times 10^{-2}$
$D_H$	water-ground friction coefficient	$\sigma^{-1} \text{m}^2 \text{yr}^{-1}$	0.05

Table 5.1: All the parameters of Equations (2.26), with their description, units and typical values.

We will also introduce a forcing term. An obvious choice would be to imitate the shikim technique, by modulating the topography function  $Z$ . Instead, we will introduce the spatial periodic forcing to the infiltration function, which imitates a periodic breaking of the biological soil crust. This has the advantage of being easier to implement numerically, and also hints that simpler and cheaper techniques can accomplish the same results as a massive topography alteration. Whichever periodic forcing choice is made, it is important that it enters the model parametrically.



### 5.1.1 Turning off the root-augmentation feedback

The turning off of the root-augmentation feedback means that in the simplified model the biomass growth rate and the soil water consumption rate will not be dependent on the biomass concentration. This is done in two steps. First, the root system of the plants will be considered to be local, i.e., a plant will not be able to capture water from neighboring regions, only soil water available at the point of space where it sits. This is accomplished by taking the limit where the minimal root-system size  $S_0$  goes to zero, and thus the kernel  $\mathcal{G}$  becomes a Dirac delta:

$$\begin{aligned} \lim_{S_0 \rightarrow 0} \mathcal{G}(\mathbf{X}, \mathbf{X}', T) &= \lim_{S_0 \rightarrow 0} \frac{1}{2\pi S_0^2} \exp \left[ -\frac{|\mathbf{X} - \mathbf{X}'|^2}{2S_0^2 (1 + EB(\mathbf{X}, T))^2} \right] \\ &= (1 + EB(\mathbf{X}))^2 \delta(\mathbf{X} - \mathbf{X}'). \end{aligned} \quad (5.1)$$

From that we have that

$$\begin{aligned} G_B(\mathbf{X}, T) &= \Lambda (1 + EB(\mathbf{X}, T))^2 W(\mathbf{X}, T) \\ G_W(\mathbf{X}, T) &= \Gamma (1 + EB(\mathbf{X}, T))^2 B(\mathbf{X}, T). \end{aligned} \quad (5.2)$$

Both the biomass growth rate  $G_B$  and the soil-water consumption rate  $G_W$  are still functions of the biomass, which means that the root-augmentation feedback is still *on*. We can think of this situation as limiting the growth of the roots strictly downwards, and not to the sides. Because the model averages over the depth axis, the size of the root system is expressed as the quantity  $EB$ . In order to turn the feedback off completely, we take the root augmentation per biomass unit  $E = 0$ . This effectively says that all plants are equally capable of uptaking water from the soil, no matter what their size. We finally have that

$$\begin{aligned} G_B(\mathbf{X}, T) &= \Lambda W(\mathbf{X}, T) \\ G_W(\mathbf{X}, T) &= \Gamma B(\mathbf{X}, T). \end{aligned} \quad (5.3)$$





### 5.1.2 Turning off the shading feedback

In order to turn off the shading feedback we assume that the evaporation rate is not diminished in any way by the presence of biomass. This is accomplished by setting  $R = 0$ , which means that  $L(\mathbf{X}, T) = N$ .

### 5.1.3 Simplified equations and rescaling

The simplified equations read

$$B_T = \Lambda W B (1 - B/K) - MB + D_B \hat{\nabla}^2 B \quad (5.4a)$$

$$W_T = \mathcal{I}H - NW - \Gamma BW + D_W \hat{\nabla}^2 W \quad (5.4b)$$

$$H_T = P - \mathcal{I}H + 2D_H \hat{\nabla} \cdot \left[ H \left( \hat{\nabla} H + \hat{\nabla} Z \right) \right]. \quad (5.4c)$$

We would like to rewrite Equations 5.4 in a non-dimensional form, in order to reduce the number of parameters. We rescale the dependent and independent variables according to

$$b = B/K \quad \rightarrow \quad B = bK \quad (5.5a)$$

$$w = W\Lambda/N \quad \rightarrow \quad W = wN/\Lambda \quad (5.5b)$$

$$h = H\Lambda/N \quad \rightarrow \quad H = hN/\Lambda \quad (5.5c)$$

$$x = X/\sqrt{D_B/M} \quad \rightarrow \quad \hat{\nabla} = \sqrt{M/D_B} \nabla \quad (5.5d)$$

$$t = MT \quad \rightarrow \quad \partial_T = \partial_t M \quad (5.5e)$$

$$z = Z\Lambda/N \quad \rightarrow \quad Z = zN/\Lambda, \quad (5.5f)$$

with  $\tau = M^{-1}$  and  $\ell = \sqrt{D_B/M}$  taken as reference time and space scaling quantities. The space derivative  $\hat{\nabla}$  with respect to the real space  $X$  will be substituted by the space derivative  $\nabla$  (no hat) with respect to the dimensionless space  $x$ . Note also that the symbol for time in years is  $T$ , while the dimensionless time is denoted by  $t$ .



Equations (5.4) now read

$$b_t = \nu w b(1 - b) - b + \nabla^2 b \quad (5.6a)$$

$$w_t = Ih - \nu w - \gamma b w + \delta_w \nabla^2 w \quad (5.6b)$$

$$h_t = p - Ih + 2\delta_h \nabla \cdot [h(\nabla h + \nabla z)], \quad (5.6c)$$

where

$$\begin{aligned} I &= \frac{\mathcal{I}}{M}, \quad \nu = \frac{N}{M}, \quad \eta = EK \\ \gamma &= \Gamma \frac{K}{M}, \quad p = P \frac{\Lambda}{MN}, \quad \delta_w = \frac{D_W}{D_B}, \quad \delta_h = D_H \frac{N}{D_B \Lambda}, \end{aligned} \quad (5.7)$$

and  $I$  reads

$$I = a \frac{b + qf}{b + q}, \quad (5.8)$$

where  $a = \frac{A}{M}$  and  $q = \frac{Q}{K}$ . Table 5.2 summarizes the rescaling of the parameters in Equations (5.6), and shows their typical values.

non-dimensional param.	conversion	value
$\nu$	$\nu = \frac{N}{M}$	$\frac{10}{3}$
$a$	$a = \frac{A}{M}$	100/3
$q$	$q = \frac{Q}{K}$	0.05
$f$	—	0.1
$\gamma$	$\gamma = \Gamma \frac{K}{M}$	$\frac{50}{3}$
$p$	$p = P \frac{\Lambda}{MN}$	$\frac{1}{150} \cdot P$
$\delta_w$	$\delta_w = \frac{D_W}{D_B}$	100
$\delta_h$	$\delta_h = D_H \frac{N}{D_B \Lambda}$	10000
$\nabla z$	$\nabla z = \hat{\nabla} \zeta \sqrt{\frac{D_B}{M} \frac{\Lambda \rho_h}{N}}$	$\hat{\nabla} \zeta \cdot 0.182574$

Table 5.2: All the non-dimensional parameters of Equations (5.6), their conversion relations, and typical values used.

The variable  $\zeta$  denotes the topography function in meters. In the simulations below, we will always use the values shown in Table 5.2, unless otherwise noted.



## 5.2 Spatially periodic forcing

In order to simulate a spatial removal of the soil crust in a spatial periodic way, we change the infiltration contrast  $f$  to:

$$f = f_0 \left( 1 + \gamma_f \frac{\cos(k_f x) + 1}{2} \right), \quad (5.9)$$

where  $f_0$  is the infiltration contrast in the absence of periodic modulation,  $\gamma_f$  is the forcing strength, and  $k_f$  is the forcing wavenumber. For instance, for a minimum infiltration contrast of  $f_0 = 0.1$  and forcing strength of  $\gamma_f = 1.0$ , the maximum infiltration contrast on bare soil produced by the crust breaking is  $f = 0.2$ . Figure 5.3 shows the periodically forced infiltration contrast.

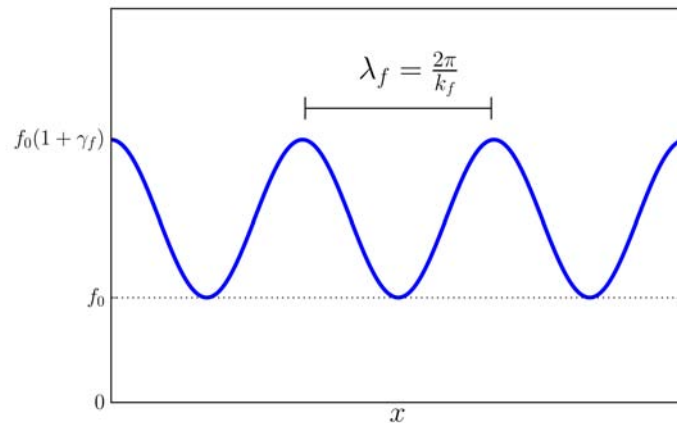


Figure 5.3: The periodically forced infiltration contrast.

## 5.3 Uniform solutions

In the absence of forcing ( $\gamma_f = 0$ ), Equations (5.4) have two uniform stationary solutions. The bare soil solution  $\mathbf{S}_0 = (b_0, w_0, h_0)$  reads

$$b_0 = 0, \quad w_0 = \frac{p}{\nu}, \quad h_0 = \frac{p}{f\alpha}. \quad (5.10)$$



and the uniform cover solution  $\mathbf{S}_u = (b_u, w_u, h_u)$  reads

$$b_u = \frac{(p-1)\nu}{\gamma + p\nu}, \quad w_u = \frac{\gamma + p\nu}{(\gamma + \nu)\nu}, \quad h_u = \frac{\gamma pq + \nu p(pq + p - 1)}{\alpha f q(\gamma + \nu p) + \alpha \nu(p - 1)}. \quad (5.11)$$

## 5.4 Linear stability analysis

We now calculate the stability ranges of the uniform solutions of the unforced ( $\gamma_f = 0$ ) vegetation system. We substitute into (5.4) the uniform solutions with non-uniform perturbation terms

$$\begin{pmatrix} b \\ w \\ h \end{pmatrix} = \begin{pmatrix} b_\star \\ w_\star \\ h_\star \end{pmatrix} + \Delta \begin{pmatrix} c_b \\ c_w \\ c_h \end{pmatrix} \cos(kx) + \Delta \begin{pmatrix} s_b \\ s_w \\ s_h \end{pmatrix} \sin(kx) \quad (5.12)$$

where  $\mathbf{S}_\star = (b_\star, w_\star, h_\star)$  denotes either  $\mathbf{S}_0$  or  $\mathbf{S}_u$ .

Keeping only linear terms in  $\Delta$ , we have the linear system

$$\frac{d}{dt}d = J(\mathbf{S}_\star)d, \quad (5.13)$$

where  $d = (c_b, c_w, c_h, s_b, s_w, s_h)^T$ . The Jacobian  $J(\mathbf{S}_\star)$  is a  $6 \times 6$  matrix given by

$$J(\mathbf{S}_\star) = \begin{pmatrix} J_0 & J_+ \\ J_- & J_0 \end{pmatrix}, \quad (5.14)$$

where both  $J_0$  and  $J_\pm$  are  $3 \times 3$  matrices that read

$$J_0 = \begin{pmatrix} (1 - 2b_\star)w_\star\nu - 1 - k^2 & (1 - b_\star)b_\star\nu & 0 \\ \frac{(f-1)h_\star q\alpha - (b_\star+q)^2 w_\star \gamma}{(b_\star+q)^2} & -b_\star\gamma - k^2\delta_w - \nu & \frac{(b_\star+f q)\alpha}{b_\star+q} \\ \frac{(f-1)h_\star q\alpha}{(b_\star+q)^2} & 0 & -\frac{\alpha(b_\star+f q)}{b_\star+q} - 2\delta_h h_\star k^2 \end{pmatrix},$$

$$J_\pm = \begin{pmatrix} 0 & 0 & 0 \\ 0 & 0 & 0 \\ 0 & 0 & \pm 2\delta_h k \nabla z \end{pmatrix}. \quad (5.15)$$



For each of the uniform solutions, we can find the eigenvalues of the Jacobian. When the real part of all eigenvalues is negative for every value of  $k$ , the solution is stable, otherwise it is unstable. Because we have a polynomial of order 6 to solve in order to find the eigenvalues, this calculation can only be done numerically for specific solutions, and unfortunately we cannot show a stability study such as the one shown in section 4.3.

## 5.5 1d solutions

The linear stability analysis of the uniform cover solution tells us that there is a finite wavenumber instability at  $p^* = 1.274$ . The uniform cover solution is linearly unstable for  $1 < p < p^*$ , and stable for  $p > p^*$ . At the bifurcation point  $p^*$  a stripe pattern solution appears with a (non-dimensional) wavenumber  $k = 0.163$ , which corresponds to a characteristic wavelength of 0.88m. We studied Equations (5.6) with the continuation software AUTO, using the parameter values shown in Table 5.2, assuming a flat and horizontal topography function, i.e.,  $\nabla z = 0$ , and without any spatial periodic forcing.

Figure 5.4 shows a bifurcation graph of the uniform solutions, with the precipitation  $p$  as the control parameter. The bare soil solution is stable for  $p < p_2 = 1$ , where it undergoes a zero wavenumber instability. At this same critical value, the uniform cover branch appears in a supercritical bifurcation. The simulation shows that at  $p^* = 1.273$ , a patterned solution emerges in a subcritical bifurcation from the uniform cover branch. This critical value is in close agreement with the value calculated from the linear stability analysis. We have two ranges of bistability: between  $p_1$  and  $p_2$  the bare soil solution and the patterned solution are stable, and between  $p^*$  and  $p_3$  the patterned solution and the uniform cover state are stable. These two ranges of bistability are marked in gray shades on the graph.

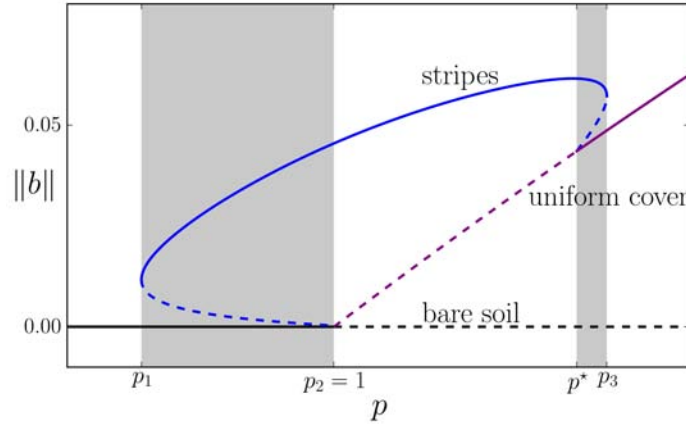


Figure 5.4: Bifurcation graph of uniform and patterned solutions. The horizontal axis indicates the control parameter  $p$ , and the vertical axis is the  $L^2$ -norm of the solutions. Bare soil, uniform and stripes solutions are shown in black, purple, and blue, respectively. Solid (dashed) lines denote stable (unstable) ranges of the solutions. Parameters:  $\nabla z = 0$ ,  $\gamma_f = 0$ .

## 5.6 2d solutions

In order to investigate 2d wavenumber locked patterns, we conducted numerical integrations of Equations (5.6), with the addition of spatially periodic forcing, as described in Section 5.2, using  $p$  as the control parameter. Once more, we used parameter values as shown in Table 5.2. Preliminary simulations showed that simulations on a horizontal topography ( $\nabla z = 0$ ) and on a flat hill slope ( $\nabla z = \text{constant}$ ) are qualitatively equal regarding the two patterned solutions discussed below. Depending on the strength of the forcing, the patterns are able to migrate uphill, while keeping their overall shape. Because of technical considerations regarding the simulations, such as meaningful criteria for determining steady state, we decided to deal only with a horizontal topography, which is easier to simulate. In addition, most of the simulations were conducted far from the finite wavenumber instability point. This means that a given pattern, e.g., the stripe pattern, has a wide range of wavenumbers for which it is stable. Preliminary simulations showed that a typical length scale of vegetation patterns is 1m, which is approximately in the middle of this range. When plotting the Fourier transform of vegetation



patterns we will draw a circle of radius  $k_0 = 0.143$ , which corresponds to the typical length scale. This circle helps us make sense of the results in the Fourier plane. The numerical integration method used is as follows: finite differences discretization of the space derivatives (the five-point stencil for the laplacian), and Euler steps to advance time. We usually stopped the simulations when they arrived at a steady state, determined when the difference of given measures of the system between two time steps, such as total biomass, were smaller than a previously decided threshold.

We found two kinds of 2d regular patterns, stripes and rectangular patterns, that are locked to the forcing wavenumber, the stripes in a 1 : 1 resonance, and the rectangular pattern in a 2 : 1 resonance. Figure 5.5 shows the  $L^2$ -norm of the biomass field as a function of precipitation, for the uniform solutions bare soil and uniform cover, and for the patterned solutions, stripes and rectangular patterns. For values of  $p < 0.75$  the only stable solution is the bare soil. In the range  $0.75 < p < 0.91$  we find that both the rectangular pattern and the bare soil are stable. Starting at  $p = 0.88$  the stripe solution also becomes stable, making the range  $0.88 < p < 0.91$  multi-stable, with rectangular patterns, stripes and bare soil. The stripe solution is stable up to  $p = 1.31$ . In the range  $1.0 < p < 1.27$  the stripe pattern is the only stable solution, and in the range  $1.27 < p < 1.31$  we find a bistable region, this time of stripes and uniform cover. For some parameter values we also found a rectangular wavenumber-locked *gap* pattern, formed by a regular array of holes in an otherwise uniform vegetation cover, but we have not produced a branch of this solution to be shown in Figure 5.5. The rectangular pattern we refer to from now on is understood as a rectangular wavenumber-locked *spot* pattern, formed by a regular array of vegetation spots in an otherwise bare soil state. The two wavenumber-locked solutions presented here, the stripe and rectangular patterns, as well as the wavenumber-locked gap pattern, are clearly analogous to the solutions of the unforced system that is able to produce spot, stripes and gap patterns, as seen in Subsection 2.2.3.

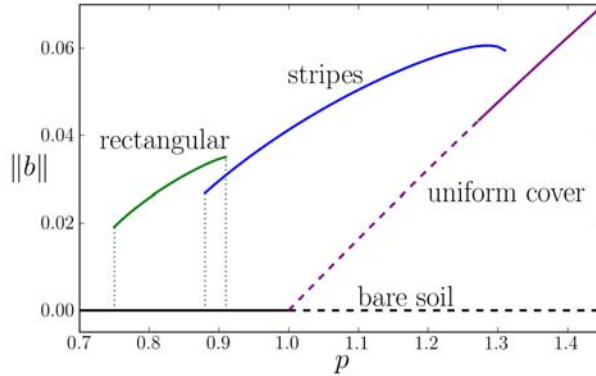


Figure 5.5: Bifurcation graph of wavenumber-locked solutions of Equations (5.6). The horizontal axis indicates the control parameter  $p$ , and the vertical axis is the  $L^2$ -norm of the biomass field of the solutions. The black and purple lines represent the bare soil solution and uniform cover solution, respectively, and their stability ranges were calculated numerically using the continuation method AUTO. The blue and green lines represent stable ranges of the stripe and rectangular patterns, respectively, calculated from numerical integrations. Parameters:  $\gamma_f = 1.0$ ,  $k_f = 1.1k_0$ .

### 5.6.1 Patterns outside their stability range

What happens when a patterned solution is taken out of its stability range? Figure 5.6 shows the evolution of a stripe pattern for the precipitation rate of  $p = 0.80$ . The biomass in the whole domain diminishes rapidly, and the rectangular solution appears from defects on the left-most stripe, and spreads to the right, finally dominating the whole system. The upper panels show the evolution of the biomass, and the lower panels show the Fourier transform. As the rectangular pattern takes over the system, we see the buildup of four wavevectors, in addition to the two wavevectors that characterized the stripe solution. The  $x$  component of these four wavevectors is half of the forcing wavenumber, which characterizes a  $2:1$  resonance. The circle in blue has a radius  $k_0 = 0.143$ , which is a typical wavenumber of the system that corresponds to the typical length of 1m. We see that the four wavevectors are located inside this circle, because their norm is smaller than  $k_0$ , which means that the typical distance between patches is slightly larger than 1m. This stems from the fact that the system has a wide band of stable modes,





and the rectangular pattern can have different scales in the  $y$  direction, while maintaining a 2 : 1 locking in the  $x$  direction.

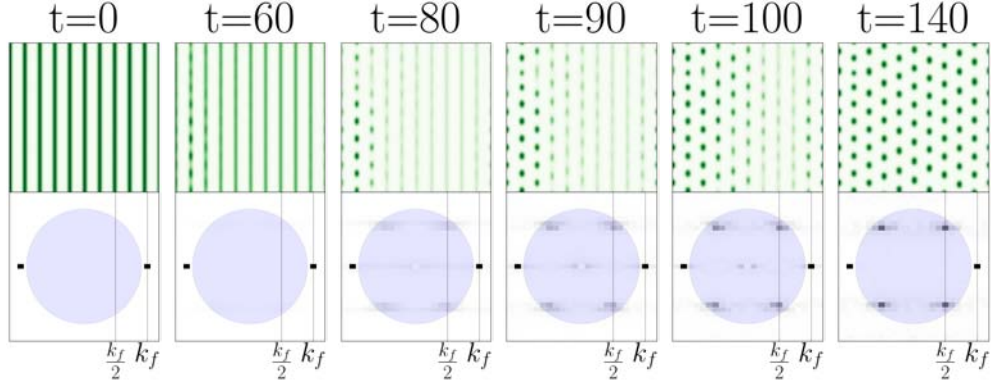


Figure 5.6: Snapshots of the evolution of a stripe pattern calculated outside of the stability region of its initial pattern. The upper panels show the biomass on a  $410 \times 410$  domain, and the lower panels depict the Fourier transform. Parameters:  $p = 0.80$ ,  $\gamma_f = 1.0$ ,  $k_f = 1.1k_0$ .

Taking the rectangular pattern out of its stability range to higher precipitation rates, we see the opposite process, namely, the rectangular pattern becomes a stripe pattern. Figure 5.7 shows the evolution of an initial condition of rectangular pattern for  $p = 1.10$ . The spots of the rectangular pattern become elongated, until they touch and form continuous stripes. There appears to be no sign of significant decay in the overall biomass. In this process, we see in the lower panels that the four wavevectors responsible for the rectangular pattern gradually disappear, leaving only the two wavevectors that form the stripe pattern.

The two processes discussed above suggest that the stripe pattern and the rectangular pattern behave very differently when taken out of their stability regions, for lower and higher precipitation rates, respectively. In order to understand this difference, we ran two series of simulations. The first series had as initial condition the steady state achieved for the rectangular pattern at the right edge of its stability range, at  $p = 0.91$ . The simulations ran for different values of  $p > 0.91$ , in the range where the stripe pattern is stable. The second series had the steady state stripe pattern as initial condition,

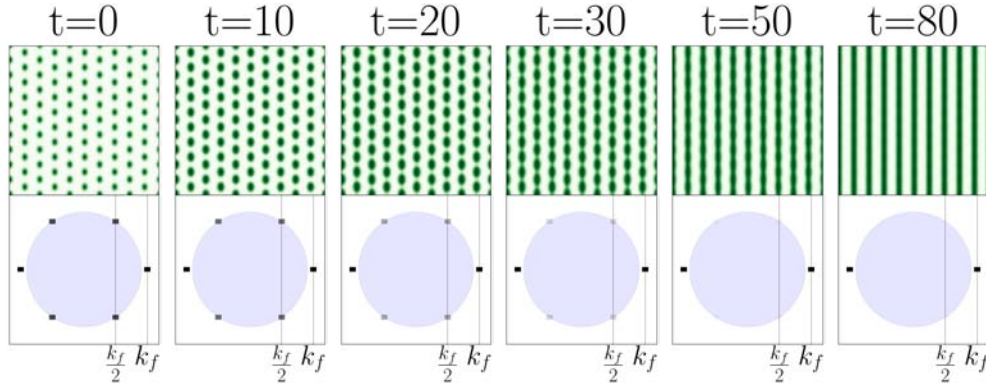


Figure 5.7: Snapshots of the evolution of a rectangular pattern calculated outside of the stability region of its initial pattern. The upper panels show the biomass on a  $199 \times 262$  domain, and the lower panels depict the Fourier transform. As the pattern changes from rectangular to stripes, we see the four wavevectors that sit on the border of the blue circle disappearing. Parameters:  $p = 1.10$ ,  $\gamma_f = 1.0$ ,  $k_f = 1.1k_0$ .

calculated at the left edge of its stability range, at  $p = 0.88$ . The simulations ran for  $p < 0.88$ , in the range where the rectangular pattern is stable. The results are shown in Figure 5.8. The top graph shows an inset of the bifurcation graph shown in Figure 5.5, with ten points marked with letters from ‘a’ to ‘j’. The points a-e represent simulations that had as initial condition the rightmost stable rectangular pattern from the rectangular branch ( $p = 0.91$ ). The points f-j represent simulations that had as initial condition the leftmost stable stripe pattern from the stripe branch ( $p = 0.88$ ). The bottom graph shows the mean biomass (dimensionless) as a function of time, scaled back to years to give a sense of how the dynamics evolves in real time (remember,  $T$  is measured in years, while  $t$  is dimensionless). The green lines show the evolution of points a-e, i.e., five simulations of the last stable rectangular solution put outside the rectangular stability range. For all the simulations, the mean biomass increases fast, and after a typical period of 10 years it stabilizes. As seen in Figure 5.7, it takes about 40 years for the spots that make up the rectangular pattern to merge. All five simulations shown ended up as stripe patterns.

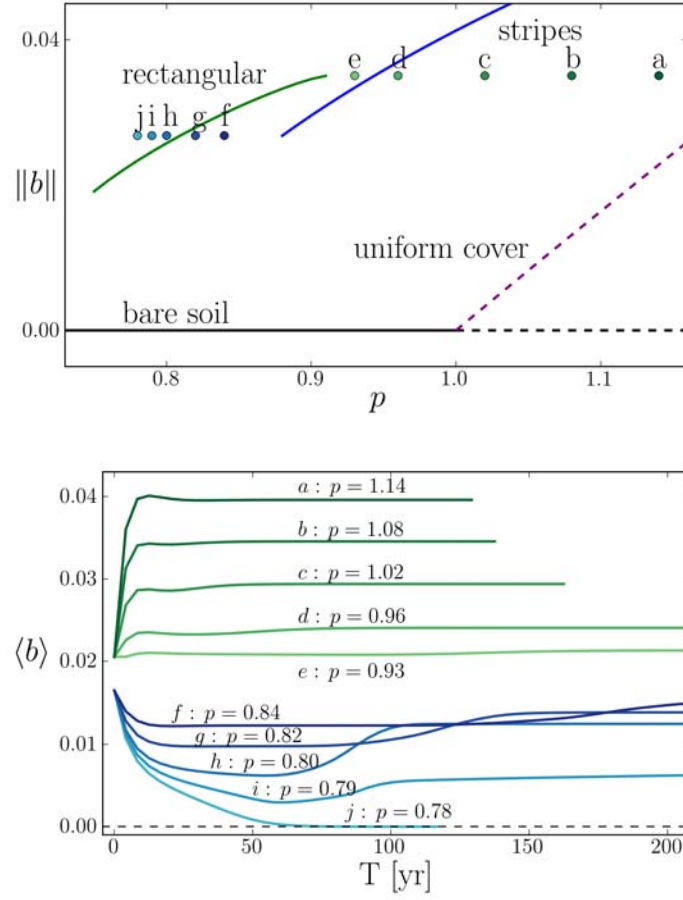


Figure 5.8: Ten simulations of the rectangular and stripe patterns taken out of their stability ranges. The figure on the top shows the points on a bifurcation graph, for rectangular initial conditions (points a-e), and for stripe initial conditions (points f-j). The bottom figure shows the evolution of the mean biomass in time for these ten points.

The blue lines show the evolution of points f-j, which are simulations of the last stable stripe solution, for decreasing values of  $p$ . For  $p = 0.84$  the mean biomass decreases monotonically, stabilizes, and at  $T \simeq 170$  rises again until it reaches a steady value at  $T \simeq 300$  (not shown in the graph), where the mean biomass corresponds to the rectangular pattern. The closest  $p$  is to the bifurcation point  $p = 0.88$ , the slower the dynamics, because of the very small eigenvalues associated with it. As the precipitation is decreased to  $p = 0.82$  and  $p = 0.80$ , we see the mean biomass falling to lower values, and



reaching a rectangular steady state in shorter time scales. This is exactly what we see in Figure 5.6, where the biomass plummets in almost the whole domain, before the rectangular pattern starts to take over. For instance, the simulation for  $p = 0.80$  has a minimum mean biomass about 50% of the value it eventually stabilizes to. The system effectively collapses, and it takes about 70 years for it to recover and be able to form the stable rectangular pattern. The simulation for  $p = 0.79$  has a collapse so thorough in most of the system that the ensuing dynamics is a slow competition between a domain of rectangular pattern that manages to survive and its bare soil surroundings. This is the reason that this curve stabilizes at mean biomass values much lower than expected for a full domain with a rectangular pattern. Although the rectangular pattern is stable for precipitation values down to  $p = 0.75$ , the stripe pattern is not able to converge to it from values of  $p = 0.78$  and lower, and the whole system collapses to the stable bare soil solution, where it stays. Figure 5.9 shows snapshots of the evolution of the biomass for the points ‘i’ ( $p = 0.79$ ) and ‘j’ ( $p = 0.78$ ).

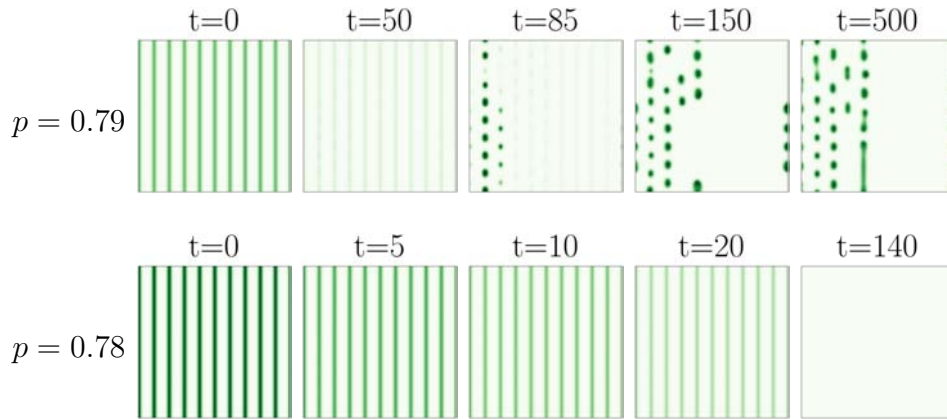


Figure 5.9: The evolution of the biomass for a stripe pattern for precipitation values  $p = 0.79$  and  $p = 0.78$ . The stripes for  $p = 0.79$  collapse, and are succeeded by front dynamics between bare soil and rectangular pattern. For  $p = 0.78$  the stripe pattern completely collapses and the system arrives at the bare soil solution as a steady state.

The results above show that a vegetation system planted with a 1 : 1 wavenumber locked stripe pattern can collapse in some regions, or even



entirely, when precipitation rates decrease. The collapse can happen even for precipitation values for which the system supports a productive state, namely, the rectangular pattern. The rectangular pattern, when taken out of its stability range towards higher precipitation values, is able to change and transform into the stripe pattern, without any loss in total productivity, and at a relatively fast time scale. We conclude that the rectangular pattern is therefore more resilient than the stripe pattern, when the system undergoes climatic rainfall fluctuations.

### 5.6.2 Front dynamics

In Figure 5.5 we have shown that the stability branch of the rectangular pattern ends at precipitation values of  $p = 0.75$ . When the precipitation is only slightly decreased from this limit value, the whole vegetation pattern collapses into the unproductive bare soil state. If precipitation is then increased to its previous value, the system stays in the unproductive state, making the transition *irreversible*. This is the basic scenario of a *catastrophic regime shift* [80]. These abrupt regime shifts can also take place more to the middle of a bistability range (in the example above for  $p > 0.75$ ), but the collapse can only happen in the unlikely case of global strong disturbances.

Within a bistability range, local strong disturbances are more probable, and they can lead to another kind of regime shift. We have seen in Figure 5.9 that for  $p = 0.79$  an initial small region of rectangular pattern expands into the bare soil, and the two domains interact via a slow front dynamics. This is the basic scenario of a *gradual regime shift* [55]: a global transition that takes place by the expansion and coalescence of domains of alternative states in a multi-stability range.

In order to understand what should be the preferred planting configurations in the rehabilitation of an unproductive area, we should investigate the dynamics of fronts between bistable solutions, and which precautions should be taken to avoid an undesirable regime shift. For three multiple stability regions, we mixed the solutions in space by forming fronts that are biasymptotic to two alternative stable states. We distinguish between two types of



such fronts, “tangential fronts”, parallel to the forcing contours and “normal fronts”, perpendicular to the forcing contours. We will now study each of the three ranges separately.

### **The range $0.75 < p < 0.88$**

In the range  $0.75 < p < 0.88$ , both the rectangular pattern and the bare soil are stable. For precipitation value  $p = 0.80$ , we mixed these two solutions in two ways, with tangential fronts along the  $y$  axis, and with normal fronts along the  $x$  axis. The three panels on the top of Figure 5.10 show that the tangential front is static, and there is no invasion. The spots that constitute the tangential fronts grow at first, because they have more water available from the bare soil region. The biomass growth stabilizes in a short time scale, of about  $t = 20$ , and then slow dynamics ensues until steady state is reached. The panels on the bottom of Figure 5.10 show that the normal front is not static, and the vegetation is able to invade the bare soil state. The simulation did not reach steady state, and the rightmost panel shows the last calculated configuration. It seems that the vegetation is able to invade by creating a solution different from the rectangular pattern, the 2:1 wavenumber locked stripe pattern. It is not clear whether the 2:1 stripes in the middle will eventually split into spots, but in any case this did not happen for time values up to 1600 years ( $t = 2000$ ).

### **The range $0.88 < p < 0.91$**

In the range  $0.88 < p < 0.91$ , we have three stable solutions, the rectangular pattern, the stripe pattern and the bare soil state. We will now discuss the dynamics of tangential and normal fronts for all three combinations of the stable solutions, for  $p = 0.89$ .

Figure 5.11 shows tangential and normal fronts between the rectangular pattern and the stripe pattern. The panels on the top show that steady state is reached at  $t = 150$  (according to a numerical convergence criterion), and we can hardly see any change compared with the initial condition, therefore the

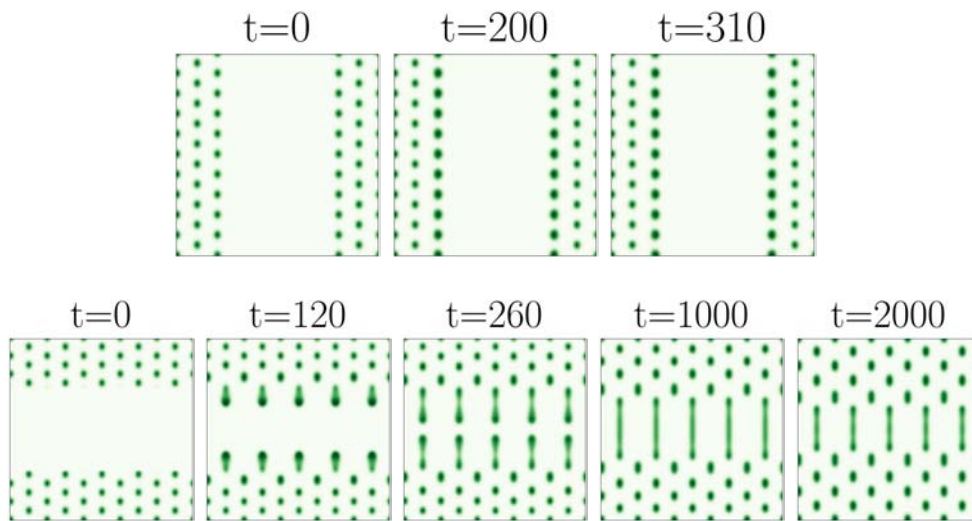


Figure 5.10: Tangential and normal fronts of rectangular and bare soil solutions, for  $p = 0.80$ . The forcing varies in the  $x$  (horizontal) direction. The panels on the top indicate that the tangential front is static, while the panels on the bottom show that vegetation can invade the bare soil solution from a normal front.

tangential front is static. The panels on the bottom show that the rectangular pattern invades the stripe pattern and ends up occupying the whole domain.

Figure 5.12 shows tangential and normal fronts between the rectangular pattern and the bare soil solution. In both cases the rectangular pattern invades the bare soil state. In the case of tangential fronts, the invasion is in waves of activity, with little expansion between them. In each wave of expansion the vegetation colonizes a new stripe region, where the infiltration contrast is maximal, forming a stripe that can break up into small patches. The last snapshot shows the steady state at  $t = 2180$ , and we identify that most of the domain is occupied by the rectangular pattern, with a few irregularities (parts of a stripe that could not split into smaller patches), and also two stripes. As we saw above, for these parameters the stripe and rectangular pattern can coexist in tangential fronts. With regard to the normal fronts, the expansion is much faster and orderly than in the case of tangential fronts. Each patch of vegetation on the border is elongated and soon after breaks up into small patches, and thus the invasion happens. In the time



scale  $t \approx 400$  the system is already fully occupied by vegetation patches, and slow dynamics then takes place, where stripes break up and patches of vegetation adjust themselves to the rectangular pattern. Although the last snapshot at  $t = 5000$  is still not the steady state, it is clear that the system converges ever so slowly to the rectangular configuration. The waves of activity in the case of tangential fronts are not clearly identifiable in the figure, because we purposely chose to show snapshots that *did* show changes, and we did not emphasize the long stretches of time when little happened to the system. We also prepared a third simulation, with an island of rectangular pattern surrounded by bare soil, as initial condition. The reader is invited to flip through the top ‘ears’ of the pages of this dissertation, and a smooth movie of the dynamics will unfold.

Figure 5.13 shows tangential and normal fronts between the stripe pattern and the bare soil solution. Once again the expansion of vegetation in the case of tangential fronts is in waves. The two stripes on the border of the stripe pattern migrate in the direction of the bare soil, but they do not split. We plotted red lines corresponding to the maximum of the forcing for the last snapshot at  $t = 910$ , which is the steady state. We see that the stripes sit roughly on the maximum of infiltration contrast, but there is no clear periodicity. On the left and right sides of the domain, we find stripes separated by one period of forcing, then a little to the center we see a separation of two periods of forcing, and finally the two stripes in the center are separated by four periods of forcing. The dynamics of the normal fronts is much faster, and in the time scale  $t \approx 250$  the whole domain is occupied by patches of vegetation. The stripes tips expand rapidly in the direction of the bare soil, and while they do so, they break up into patches. The breakup into patches also affects the part of the stripes that were initially further from the bare soil. The vegetation patches move slowly and finally we see that the steady state at  $t = 3830$  has a rectangular configuration.



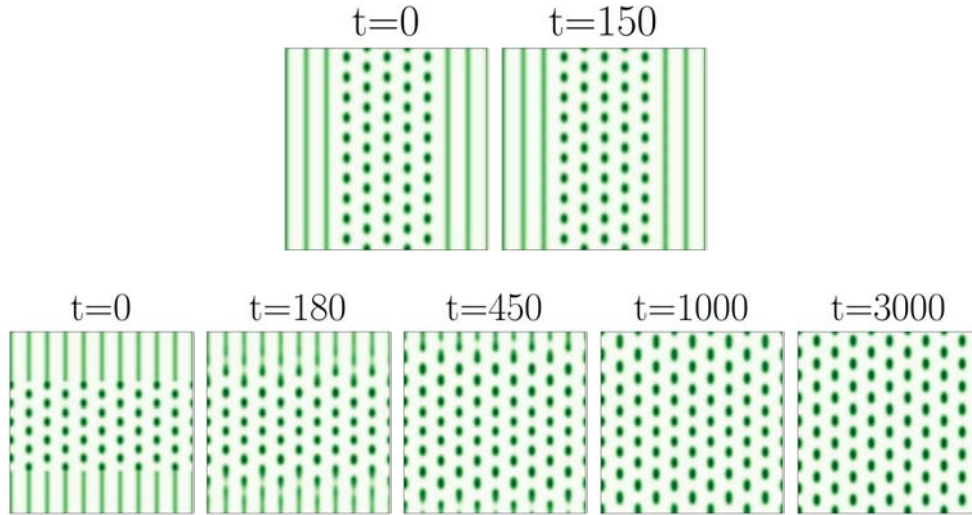


Figure 5.11: Tangential and normal fronts of rectangular and stripe solutions, for  $p = 0.89$ . The panels on the top indicate that the tangential front is static, while the panels on the bottom show that the rectangular solution invades the stripe pattern.

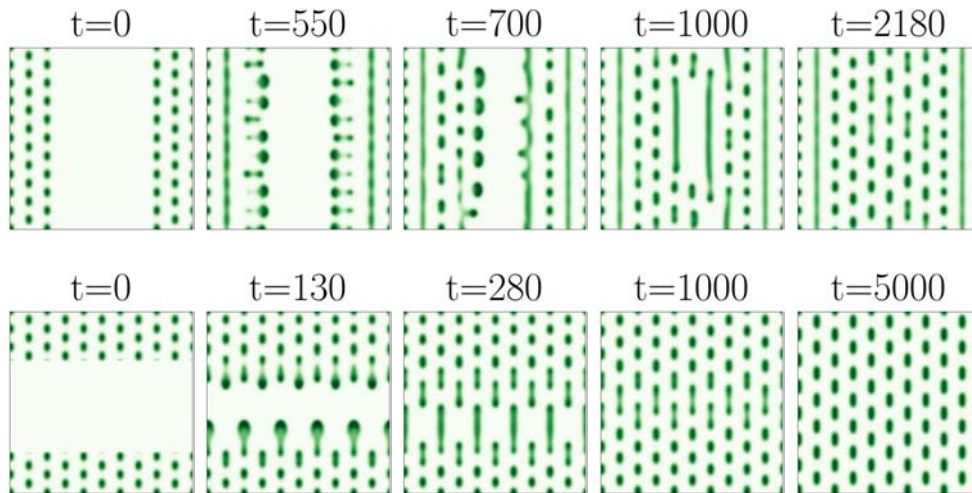


Figure 5.12: Tangential and normal fronts of rectangular and bare soil solutions, for  $p = 0.89$ . In both cases the vegetation invades the bare soil region, and the system converges to the rectangular pattern (albeit with some defects and stripe regions in the case of tangential fronts).



### **The range $0.91 < p < 1.00$**

In the range  $0.91 < p < 1.00$  there are two stable solutions, the stripe pattern and the bare soil state. The stripes on the border of the tangential front move in the direction of the bare soil, split, and end up occupying the whole domain, but the steady state is not a 1 : 1 stripe solution. We plotted red lines corresponding to the maximum of the forcing for the last snapshot, and we see that the vegetation stripes sit roughly on the maximum of infiltration contrast, but there is no clear periodicity. In the case of the normal front, the stripe pattern rapidly invades the bare soil, and the steady state is a 1 : 1 stripe pattern.

### **General features**

We have investigated separately the mixing of two bistable states with tangential and normal fronts, but in general the front between domains of solutions in nature contains both kinds of fronts. We have seen that the rectangular pattern could always invade the stripe and bare soil solutions, for all bistability regions. The bare soil solution was always invaded by vegetation. These outcomes are significant for gradual regime shifts, because they indicate that spatial periodic forcing is indeed an effective procedure to reverse desertification. In all bistability regions of bare soil and a vegetated state (stripe and rectangular), we expect even a small patch of vegetation to grow and slowly colonize the whole bare soil state.

## **5.7 Preventive measures**

The results above are extremely relevant for guiding rehabilitation efforts. When using periodic forcing methods such as the shikim technique, periodic breaking of the soil crust as discussed here, or other methods, one should take into account environmental changes, such as varying precipitation rates. The results indicate that the rectangular pattern represents a more resilient vegetation state than the usually preferred 1 : 1 stripe pattern, because it

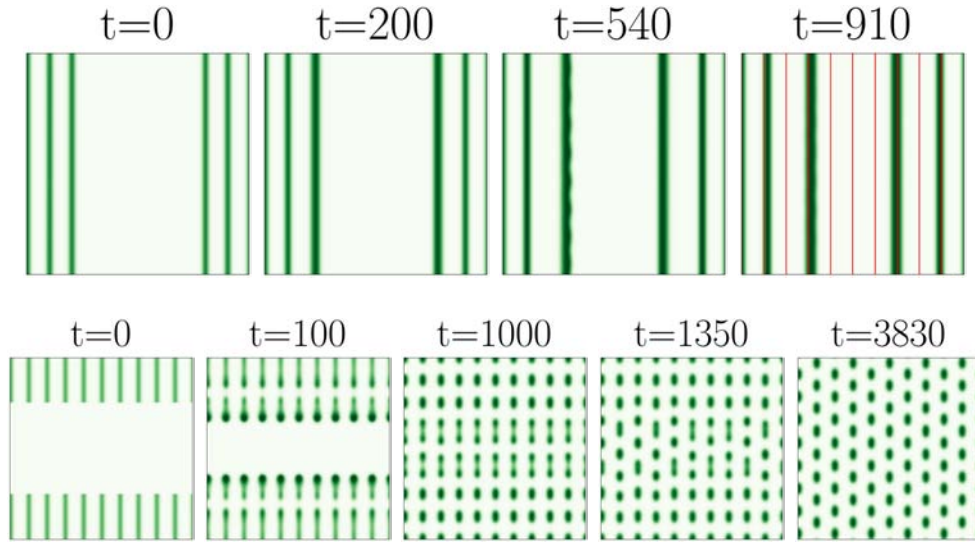


Figure 5.13: Tangential and normal fronts of stripe pattern and bare soil solutions, for  $p = 0.89$ . In the case of tangential fronts, the stripes migrate and the steady state consists of a stripe pattern with no clear periodicity. When the front is normal, the steady state is a rectangular pattern.

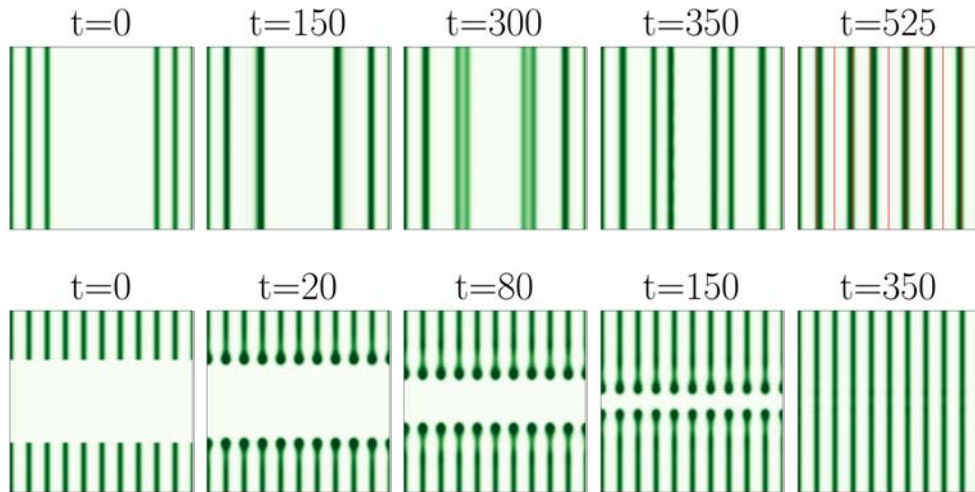


Figure 5.14: Tangential and normal fronts of stripe pattern and bare soil solutions, for  $p = 0.95$ . While in the case of normal fronts the steady state is a 1 : 1 wavenumber locked stripe pattern, in the case of tangential fronts, the steady state is a stripe pattern with no clear periodicity.



is suitable for low precipitation values, and can easily adapt itself to stripe patterns for higher  $p$  values. When planning the planting of vegetation using spatial periodic forcing, one should prefer the rectangular pattern over the stripe pattern, in order to avoid a great decrease in the system's biomass, or even a complete collapse to the bare soil state. The results also suggest that preventive actions can be taken before the collapse of a stripe pattern configuration. Near the tip of its stability range, a vegetation system with a stripe pattern configuration should experience *critical slowing down*. This slowing down can manifest itself in the increase of temporal autocorrelation and variance [81, 82, 83], and in the skewness of time-series distributions [84]. When these signs can be identified, it would be advisable to remove part of the biomass along the stripes, so it more resembles the stabler rectangular configuration. The conversion of stripes into a rectangular pattern would not mean a compromise in total productivity, because, although the vegetation cover of the rectangular pattern is smaller, each vegetation patch reaches higher biomass densities than those found on a stripe pattern. Figure 5.15 shows that the mean biomass of the rectangular pattern is slightly higher than that of the stripe pattern, throughout their bistability range.

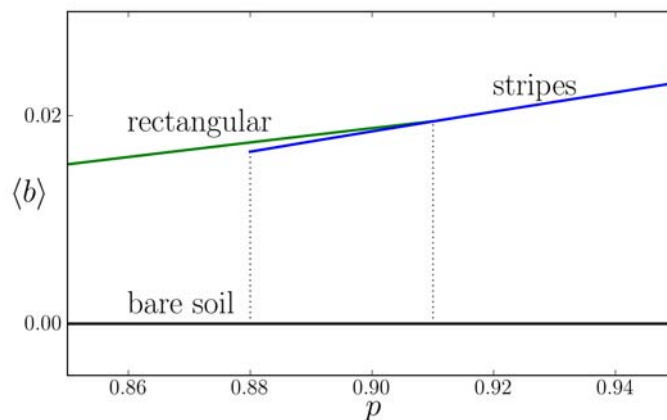


Figure 5.15: The mean biomass as a function of the precipitation rate, for the rectangular and stripe patterns. Although the rectangular pattern appears to have lower coverage, its total biomass is similar and even slightly higher than that of stripes.



## 5.8 Comparison with the SH model

In what ways are the simplified vegetation model and the parametrically forced SH model similar? Can the resonant patterns in the vegetation system be described qualitatively by the SH model?

Similarly to the parametrically forced SH model, the simplified vegetation model also has 1 : 1 resonant stripes and 2 : 1 resonant rectangular solutions. The rectangular pattern of the vegetation model is also able to adjust itself to a wide range of forcing wavenumbers. Figure 5.16 shows four solutions, with their respective Fourier transform. For  $k_f = 0.70k_0$ , the four wavevectors responsible for the rectangular pattern sit on the border of a circle of radius  $k_0 = 0.143$ , and their component in the  $Q_x$  direction is exactly  $k_f/2$ . We find two wavevectors with high absolute value of the Fourier transform inside the blue circle, which represent the forcing, with  $\mathbf{k} = \pm k_f \hat{x}$ . There are also other ‘weaker’ wavevectors outside the blue circle that are harmonics of the six wavevectors discussed above. As  $k_f$  is increased, the four ‘rectangular’ wavevectors become stronger and migrate on the border of the blue circle, always maintaining their component in the  $x$  direction locked in a 2 : 1 resonance with the forcing. The two wavevectors located at  $\pm k_f \hat{x}$  also migrate to the outer region on the blue circle. The wavevectors corresponding to the harmonics are still present, but do not appear in the pictures presented.

The wavevectors  $\mathbf{k} = \pm k_f \hat{x}$  that are present in the vegetation model’s rectangular pattern are not seen in the SH model’s rectangular pattern. These wavevectors make the vegetation’s rectangular pattern resemble a hexagonal pattern. In fact, the vegetation model can exhibit hexagonal solutions when no forcing is applied, while the SH model cannot. This is the result of the fact that the SH model has an up-down symmetry, i.e., Equation (2.1) is invariant to the transformation  $u \rightarrow -u$ . A stripe pattern of the SH model is unchanged with the inversion of  $u$ , but a hexagonal pattern corresponding to spots would become another pattern, a hexagonal pattern that corresponds to holes. A quadratic term of the kind  $\lambda u^2$  can be added to the SH model in order to break the up-down symmetry, and thus allow for hexagonal patterns. The parametrically forced SH equation without up-down

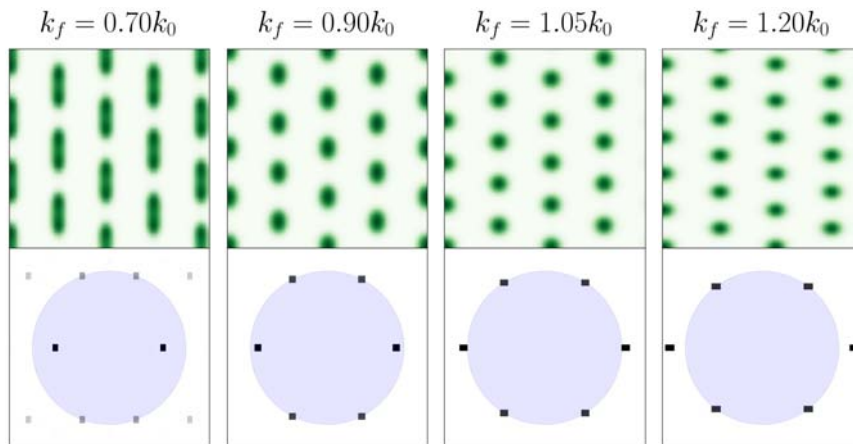


Figure 5.16: Four rectangular patterns calculated for different values of forcing wavenumber. The upper panels show the biomass on a  $200 \times 200$  domain, and the lower panels depict the Fourier transform. The four wavevectors responsible for the rectangular pattern always sit on the border of the blue circle, whose radius is  $k_0 = 0.143$ , while the two strong wavevectors  $\mathbf{k} = \pm k_f \hat{x}$  can be found either inside or outside it. Parameters:  $p = 0.80$ ,  $\gamma_f = 1.0$ .

symmetry reads

$$\partial_t u = [\epsilon + \gamma \cos(k_f x)] u + \lambda u^2 - u^3 - (\nabla^2 + k_0^2) u. \quad (5.16)$$

In order to distinguish it from Equation (2.8) we will call Equation (5.16) SH23, because it has both quadratic and cubic nonlinear terms.

Figure 5.17 shows two rectangular patterns and their Fourier transform, for the parametrically forced SH23 equation (5.16), and for the simplified vegetation model. As we can see, the Fourier transforms of both patterns are very similar: both have four wavevectors that sit on a circle of radius  $k_0$  (whose value is different for each model), and two wavevectors located at  $\mathbf{k} = \pm k_f \hat{x}$ . Equation (5.16) seems more suitable for modeling real-life systems that lack the up-down symmetry, and a detailed analysis of it, much as was done in chapters 3 and 4 can shed light on the processes in play in the vegetation model studied here.

Furthermore, although the vegetation model is much more complex than



the SH model, and we do not know if it has a Lyapunov functional, the front dynamics appears to behave as if it does. The rectangular pattern behaves as if it has the lowest energy, and the bare soil the highest, in the precipitation ranges of multiple stability. The fronts between multiple stable states were simulated for a few points in a multi-dimensional parameter space. Because we cannot write an energy functional for the vegetation model, it is hard to generalize the results found in this chapter. A comprehensive study of the energy functional of the solutions of the SH23 can help us understand the front dynamics of the analogous solutions of the vegetation model.

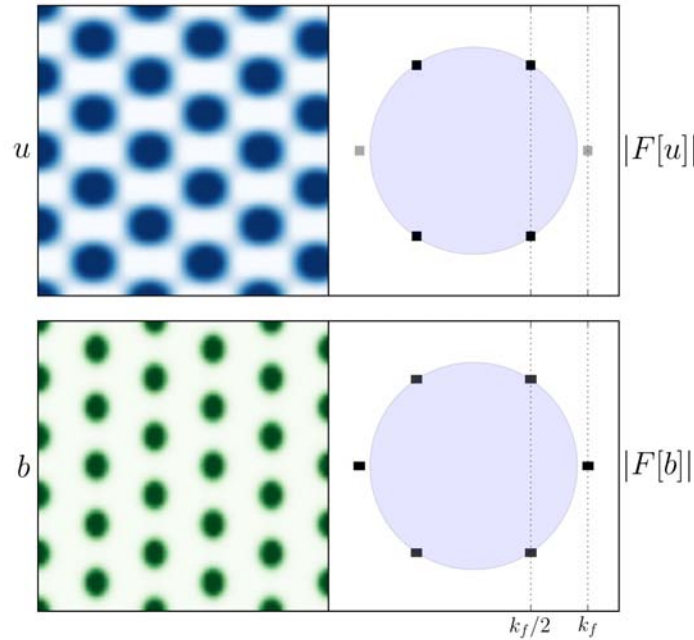


Figure 5.17: Two rectangular patterns, and their Fourier transform. The panels on the top correspond to a solution of the forced SH23 Equation (5.16), and the panels on the bottom correspond to a solution of the forced simplified vegetation model. Parameters for the panels on the top:  $\epsilon = 0.1$ ,  $\lambda = 0.3$ ,  $\gamma = 0.1$ ,  $k_f = 1.1k_0$ ,  $k_0 = 1.0$ . Parameters for the panels on the bottom:  $p = 0.80$ ,  $k_f = 1.1k_0$ ,  $k_0 = 0.143$ .



## Chapter 6

## Conclusion

*“The important thing in science is not so much to obtain new facts as to discover new ways of thinking about them.”*

– William Lawrence Bragg

In this dissertation we investigated the effects of spatial periodic forcing on pattern forming systems. We took the simplest system that undergoes a finite wavenumber instability, the Swift-Hohenberg equation, and added to it a parametric forcing term. We found that in one space dimension, the forcing is able to bring forth wavenumber locked solutions, whose wavenumber  $k$  is entrained by the forcing wavenumber  $k_f$  in such a way that the relation  $k = nk_f$  is fixed. The forcing is always able to increase the stability region of patterned solutions in the parameter space, even in regions below the threshold of pattern formation of the unforced system ( $\epsilon < 0$ ), provided that a minimal forcing  $\gamma$  strength is applied.

In two-dimensional domains, oblique and rectangular patterns exist and are stable for a very wide range of forcing wavenumbers. These 2d patterns dramatically change the stability range of stripe patterns, determining a critical value  $\epsilon_c$  below which the stripe solution is unstable in a range of forcing strength  $\gamma$ , even when  $k_f$  equals the system’s natural wavenumber. This seems counter-intuitive because naïvely we would expect the 1:1 forcing to reinforce the stripe pattern, as in the 1d case. In 2d, though, the system





can yield more easily to the forcing by responding in the orthogonal direction through the growth of oblique modes that destabilize stripe patterns. We also found that even when the forcing leaves the stripes linearly stable, the 1 : 1 stripes are displaced by the 2d patterns that the forcing induces.

In Chapter 5 we presented a simplified vegetation model for water-limited systems. We introduced spatial forcing by a periodic modulation of the infiltration contrast, which corresponds to a periodic removal of the soil crust. In a 2d domain we found, besides the bare soil solution and the uniform cover solution, wavenumber-locked solutions: a stripe pattern in a 1 : 1 resonance and a rectangular solution in a 2 : 1 resonance. The rectangular pattern was found to be more versatile than the usually preferred 1 : 1 stripe pattern, because it is stable for lower precipitation values and can adjust itself easily to a stripe pattern for higher values of  $p$ . On the other hand, the stripe pattern, when taken out of its range of stability towards lower  $p$  values, tends to collapse, and the transition to the rectangular pattern can be slow, or not even happen. Simulations between bistable solutions showed that the vegetation system behaves as if it had an energy functional, and the rectangular pattern could always invade either the bare soil or the stripe solution.

These findings indicate that in rehabilitation efforts of drylands by spatial periodic water-harvesting techniques, the rectangular pattern should be preferred to the usual 1 : 1 stripe pattern. Moreover, a preventive measure to avoid the collapse of the whole system is the removal of part of the stripe's biomass, so the pattern resembles more the stabler rectangular pattern.

Future work should investigate the solutions of the Swift-Hohenberg equation with quadratic and cubic terms. This is a more generic pattern-forming system, and it should better describe other systems in nature that lack the up-down symmetry.

The mathematical approach to rehabilitation of drylands, and the recasting of spatial periodic water-harvesting techniques as a parametric resonance problem are still in their incipient stages. We hope that this work can be used as a stepping stone to further development in the modeling of periodically forced vegetation systems, and of periodically forced pattern-forming



## Chapter 6. Conclusion

---

systems in general.



# Appendix A

## Semi-spectral method for PDEs

*“An algorithm must be seen to be believed.”*

– Donald Knuth

The semi-spectral method is extremely useful when working with reaction-diffusion systems, and with parabolic PDEs in general. This was the method used to run all the simulations of the Swift-Hohenberg model in this thesis, and it proved to be reliable and fast. The explanation below is a summary of “Spectral algorithms for reaction-diffusion equations”, by Richard V. Craster and Roberto Sassi [85], with a step by step recipe, so the reader can easily apply the method to any suitable problem.

### A.1 The method

The semi-spectral transform method is very useful when we have to integrate a system that evolves really slowly. Let us say we have a (parabolic) system of the form:

$$u_t = \epsilon u + f(u) + D\nabla^2 u, \quad (\text{A.1})$$

where  $f(u)$  is a nonlinear function. First, we compute the Fourier transform of (A.1):

$$\hat{u}_t = \epsilon \hat{u} + \hat{f}(u) - k^2 D \hat{u}, \quad (\text{A.2})$$

where the hat denotes the Fourier transform.



## Appendix A. Semi-spectral method for PDEs

---

We rearrange (A.2) in the following way:

$$\hat{u}_t + a\hat{u} = \hat{f}(u), \quad (\text{A.3})$$

where  $a = -\epsilon + k^2 D$ , and now we make a variable substitution

$$\hat{v}(k, t) = \hat{u}(k, t) e^{at} \quad (\text{A.4a})$$

$$\hat{v}_t = \hat{u}_t e^{at} + a\hat{u} e^{at}. \quad (\text{A.4b})$$

We multiply (A.3) by  $e^{at}$  and we finally get

$$\hat{v}_t = e^{at} \hat{f}(u). \quad (\text{A.5})$$

We can now advance  $\hat{v}$  in time using a simple Euler step

$$\hat{v}^{t_{n+1}} = \hat{v}^{t_n} + \Delta t \left( e^{at_n} \hat{f}(u) \right). \quad (\text{A.6})$$

What we really want is  $\hat{u}$ , which, according to (A.4a), is given by

$$\hat{u}^{t_{n+1}} = \hat{v}^{t_{n+1}} e^{-at_{n+1}} \quad (\text{A.7a})$$

$$= \hat{v}^{t_{n+1}} e^{-at_n} e^{-a\Delta t} \quad (\text{A.7b})$$

$$= \left( \hat{v}^{t_n} + \Delta t e^{at_n} \hat{f}(u) \right) e^{-at_n} e^{-a\Delta t} \quad (\text{A.7c})$$

$$= \left( \hat{v}^{t_n} e^{-at_n} + \Delta t e^{at_n} \hat{f}(u) e^{-at_n} \right) e^{-a\Delta t} \quad (\text{A.7d})$$

$$= \left( \hat{u}^{t_n} + \Delta t \hat{f}(u) \right) e^{-a\Delta t}. \quad (\text{A.7e})$$

There is actually no need to use the variable substitution in (A.4). We now have an expression for  $\hat{u}^{t_{n+1}}$ :

$$\hat{u}^{t_{n+1}} = \left( \hat{u}^{t_n} + \Delta t \hat{f}(u) \right) e^{-a\Delta t}. \quad (\text{A.8})$$

Now it is time to go back from the Fourier space to the real space, and for that we use an inverse Fourier transform

$$u^{t_{n+1}} = \mathcal{F}^{-1}[\hat{u}^{t_{n+1}}]. \quad (\text{A.9})$$



## A.2 Step by step

To implement this technique, one just has to follow the steps below:

1. Calculate the Fourier transform of  $u$ :  $\hat{u} = \mathcal{F}[u]$ .
2. Have  $f(u)$  calculated and then take its Fourier transform:  $\hat{f}(u) = \mathcal{F}[f(u)]$ .
3. For a given lattice with  $N$  points, and  $\delta x$  being the distance between them, make the frequency bin vector (matrix)  $k$  for your one (two) dimensional system. In python the command would be `numpy.fft.fftfreq(N, dx)`. The frequency bin vector  $k$  looks like:

$$\begin{aligned}
 k &= 2\pi \cdot [0, 1, \dots, \frac{N}{2} - 1, -\frac{N}{2}, \dots, -1] / (N \delta x), & \text{if } N \text{ is even;} \\
 k &= 2\pi \cdot [0, 1, \dots, \frac{N-1}{2}, -\frac{N-1}{2}, \dots, -1] / (N \delta x), & \text{if } N \text{ is odd.}
 \end{aligned}$$

Remember that the domain size is given by  $L = N \delta x$ , which means that the denominator in the expressions above can be written simply as  $L$ . It is clear from that fact that  $\delta k$ , the tiniest slice of the Fourier space is  $\delta k = 2\pi/L$ . Corollary: if you want to divide the Fourier space into very many parts, simply have a huge domain.

If the system is two-dimensional, then have  $k_x$  and  $k_y$  calculated separately. The domain might not be square ( $L_x \neq L_y$ ), and you might want to divide the domain into a different number of points ( $N_x \neq N_y$ ). Anyway, prepare one-dimensional arrays of  $k_x$  and  $k_y$  as explained above, and then make an *outer product* of these arrays with a *ones* array of length  $N$ , as following:

$$k_{x,2d} = \begin{pmatrix} 1 \\ 1 \\ \vdots \\ 1 \end{pmatrix} \begin{pmatrix} k_{x1} & k_{x2} & \dots & k_{xN} \end{pmatrix} = \begin{pmatrix} k_{x1} & k_{x2} & \dots & k_{xN} \\ k_{x1} & k_{x2} & \dots & k_{xN} \\ \vdots & \vdots & \vdots & \vdots \\ k_{x1} & k_{x2} & \dots & k_{xN} \end{pmatrix} \quad (\text{A.11})$$



and

$$k_{y,2d} = \begin{pmatrix} k_{x1} \\ k_{x2} \\ \vdots \\ k_{xN} \end{pmatrix} \begin{pmatrix} 1 & 1 & \dots & 1 \end{pmatrix} = \begin{pmatrix} k_{y1} & k_{y1} & \dots & k_{y1} \\ k_{y2} & k_{y2} & \dots & k_{y2} \\ \vdots & \vdots & & \vdots \\ k_{yN} & k_{yN} & & k_{yN} \end{pmatrix}. \quad (\text{A.12})$$

Then factor  $e^{-a\Delta t}$  equals

$$e^{-a\Delta t} = e^{[\epsilon - D(k_x^2 + k_y^2)]\Delta t},$$

where  $k_x^2$  is the element-wise exponentiation of the 2d array  $k_{x,2d}$ .

4. Now that we have all the factors we need, we simply calculate

$$\hat{u}^{t_{n+1}} = \left( \hat{u}^{t_n} + \Delta t \hat{f}(u) \right) e^{[\epsilon - D(k_x^2 + k_y^2)]\Delta t}. \quad (\text{A.13})$$

5. We finally go back to the real space by applying the inverse Fourier transform:  $u^{t_{n+1}} = \mathcal{F}^{-1}[\hat{u}^{t_{n+1}}]$ .

### A.3 Example

For the parametrically forced Swift-Hohenberg equation (2.8) we have

$$f(u) = -u^3 + \gamma u \cos(k_f x), \quad a = \epsilon - (k_0 - k_x^2 - k_y^2)^2. \quad (\text{A.14})$$



# Bibliography

- [1] Thomas Gregor, William Bialek, Rob R de Ruyter van Steveninck, David W Tank, and Eric F Wieschaus. Diffusion and scaling during early embryonic pattern formation. *Proceedings of the National Academy of Sciences of the United States of America*, 102(51):18403–18407, 2005.
- [2] Jonathon Howard, Stephan W Grill, and Justin S Bois. Turing’s next steps: the mechanochemical basis of morphogenesis. *Nature Reviews Molecular Cell Biology*, 12(6):392–398, 2011.
- [3] J. Jalife, M. Delmar, J. Anumonwo, O. Berenfeld, and J. Kalifa. *Rotors, Spirals, and Scroll Waves in the Heart*. Wiley-Blackwell, 2009.
- [4] Mitsugu Matsushita and Hiroshi Fujikawa. Diffusion-limited growth in bacterial colony formation. *Physica A*, 168(1):498 – 506, 1990.
- [5] E. Ben-Jacob, O. Shochet, A. Tenenbaum, I. Cohen, A. Czirók, and T. Vicsek. Generic modelling of cooperative growth patterns in bacterial colonies. *Nature*, 368:46–49, 1994.
- [6] A.A. Golovin and A.A. Nepomnyashchy (eds.). *Self-Assembly, Pattern Formation and Growth Phenomena in Nano-Systems*. Springer, 2006.
- [7] E.M. Sam, Y. Hayase, G.K. Auernhammer, and D. Vollmer. Pattern formation in phase separating binary mixtures. *Phys. Chem. Chem. Phys.*, 13:13333–13340, 2011.
- [8] M. Lappa. *Thermal Convection: Patterns, Evolution and Stability*. Wiley, 2010.



## BIBLIOGRAPHY

---

- [9] F.T. Arecchi, S. Boccaletti, and P.L. Ramazza. Pattern formation and competition in nonlinear optics. *Physics Reports*, 318:1–83, 1999.
- [10] R. Kapral and K. Showalter. *Chemical Waves and Patterns*. Springer, 1995.
- [11] Katharina Krischer. Principles of temporal and spatial pattern formation in electrochemical systems. In B. E. Conway, J. O’M. Bockris, and Ralph E. White, editors, *Modern Aspects of Electrochemistry*, volume 32 of *Modern Aspects of Electrochemistry*, pages 1–142. Springer US, 2002.
- [12] G. Feingold, I. Koren, H. Wang, H. Xue, and W.A. Brewer. Precipitation-generated oscillations in open cellular cloud fields. *Nature*, 466:849–852, 2010.
- [13] V. Deblauwe, B. Barbier, P. Couteron, O. Lejeune, and J. Bogaert. The global biogeography of semi-arid. *Global Ecol. Biogeogr.*, 17:715–723, 2008.
- [14] Lucas Goehring, L. Mahadevan, and Stephen W. Morris. Nonequilibrium scale selection mechanism for columnar jointing. *PNAS*, 106(2):387–392, 2009.
- [15] Seong-min Hwang, Tae Yun Kim, and Kyoung J. Lee. Complex-periodic spiral waves in confluent cardiac cell cultures induced by localized inhomogeneities. *PNAS*, 102(29):10363–10368, 2005.
- [16] R Seemann, S Herminghaus, and K Jacobs. Gaining control of pattern formation of dewetting liquid films. *Journal of Physics: Condensed Matter*, 13(21):4925, 2001.
- [17] Cornelia Denz, Michael Schwab, and Carsten Weidmann. *Transverse-Pattern Formation in Photorefractive Optics*, volume 188. Springer, 2003.
- [18] L. G. Stanton and A. A. Golovin. Global feedback control for pattern-forming systems. *Phys. Rev. E*, 76:036210, 2007.





## BIBLIOGRAPHY

---

- [19] A.S. Mikhailov and K. Showalter. Control of waves, patterns and turbulence in chemical systems. *Phys. Rep.*, 425:79 – 194, 2006.
- [20] Mary Lowe, JP Gollub, and TC Lubensky. Commensurate and incommensurate structures in a nonequilibrium system. *Physical Review Letters*, 51(9):786–789, 1983.
- [21] Gabriel Seiden, Stephan Weiss, Jonathan H McCoy, Werner Pesch, and Eberhard Bodenschatz. Pattern forming system in the presence of different symmetry-breaking mechanisms. *Physical Review Letters*, 101(21):214503, 2008.
- [22] Milos Dolnik, Tamás Bánsági, Sama Ansari, Ivan Valent, and Irving R Epstein. Locking of turing patterns in the chlorine dioxide–iodine–malonic acid reaction with one-dimensional spatial periodic forcing. *Physical Chemistry Chemical Physics*, 13(27):12578–12583, 2011.
- [23] Sten Rüdiger, Ernesto M Nicola, Jaume Casademunt, and Lorenz Kramer. Theory of pattern forming systems under traveling-wave forcing. *Physics Reports*, 447(3):73–111, 2007.
- [24] PL Kapitza. Pendulum with a vibrating suspension. *Usp. Fiz. Nauk*, 44(5):7–20, 1951.
- [25] Diego A Golombek and Ruth E Rosenstein. Physiology of circadian entrainment. *Physiological Reviews*, 90(3):1063–1102, 2010.
- [26] VS Anishchenko, AG Balanov, NB Janson, NB Igosheva, and GV Bordyugov. Entrainment between heart rate and weak noninvasive forcing. *International Journal of Bifurcation and Chaos*, 10(10):2339–2348, 2000.
- [27] Carl Graves, Leon Glass, Donald Laporta, Roger Meloche, and Alex Grassino. Respiratory phase locking during mechanical ventilation in anesthetized human subjects. *American Journal of Physiology-Regulatory, Integrative and Comparative Physiology*, 250(5):R902–R909, 1986.



## BIBLIOGRAPHY

---

- [28] Jeppe Sturis, Carsten Knudsen, Niall M O'Meara, Jesper S Thomsen, Erik Mosekilde, Eve Van Cauter, Kenneth S Polonsky, et al. Phase-locking regions in a forced model of slow insulin and glucose oscillations. *Chaos (Woodbury, NY)*, 5(1):193, 1995.
- [29] IG Kevrekidis, R Aris, and LD Schmidt. The stirred tank forced. *Chemical Engineering Science*, 41(6):1549–1560, 1986.
- [30] M Eiswirth and G Ertl. Forced oscillations of a self-oscillating surface reaction. *Physical Review Letters*, 60:1526–1529, 1988.
- [31] Anna L Lin, Aric Hagberg, Ehud Meron, and Harry L Swinney. Resonance tongues and patterns in periodically forced reaction-diffusion systems. *Physical Review E*, 69(6):066217, 2004.
- [32] Anna L Lin, Matthias Bertram, Karl Martinez, Harry L Swinney, Alexandre Ardelea, Graham F Carey, et al. Resonant phase patterns in a reaction-diffusion system. *Physical Review Letters*, 84(18):4240–4243, 2000.
- [33] PM Varangis, Athanasios Gavrielides, Thomas Erneux, Vassilios Kovanis, and LF Lester. Frequency entrainment in optically injected semiconductor lasers. *Physical Review Letters*, 78(12):2353–2356, 1997.
- [34] Alexander N Pisarchik, Yuri O Barmenkov, and Alexander V Kir'yanov. Phase and frequency locking in a pump-modulated erbium-doped fiber laser. In *Advanced Solid-State Photonics*. Optical Society of America, 2004.
- [35] P. Coulet, J. Lega, B. Houchmanzadeh, and J. Lajzerowicz. Breaking chirality in nonequilibrium systems. *Phys. Rev. Lett.*, 65:1352, 1990.
- [36] C. Elphick, A. Hagberg, E. Meron, and B. Malomed. On the origin of traveling pulses in bistable systems. *Phys. Lett. A*, 230:33–37, 1997.
- [37] Christian Elphick, Aric Hagberg, and Ehud Meron. Phase front instability in periodically forced oscillatory systems. *Physical Review Letters*, 80(22):5007, 1998.



## BIBLIOGRAPHY

---

- [38] Christian Elphick, Aric Hagberg, and Ehud Meron. Multiphase patterns in periodically forced oscillatory systems. *Physical Review E*, 59(5):5285, 1999.
- [39] Bradley Marts, Aric Hagberg, Ehud Meron, and Anna L. Lin. Resonant and non-resonant patterns in forced oscillators. *Chaos*, 16:037113, 2006.
- [40] Arik Yochelis, Aric Hagberg, Ehud Meron, Anna L Lin, and Harry L Swinney. Development of standing-wave labyrinthine patterns. *SIAM Journal on Applied Dynamical Systems*, 1(2):236–247, 2002.
- [41] Arik Yochelis, Christian Elphick, Aric Hagberg, and Ehud Meron. Two-phase resonant patterns in forced oscillatory systems: Boundaries, mechanisms and forms. *Physica D: Nonlinear Phenomena*, 199(1):201–222, 2004.
- [42] Arik Yochelis, Christian Elphick, Aric Hagberg, and Ehud Meron. Frequency locking in extended systems: The impact of a turing mode. *EPL (Europhysics Letters)*, 69(2):170, 2005.
- [43] P Coulet. Commensurate-incommensurate transition in nonequilibrium systems. *Physical Review Letters*, 56:724–727, 1986.
- [44] G Freund and W Zimmermann. Rayleigh–bénard convection in the presence of spatial temperature modulations. *Journal of Fluid Mechanics*, 673:318–348, 2011.
- [45] R Neubecker and A Zimmermann. Spatial forcing of spontaneous optical patterns. *Physical Review E*, 65(3):035205, 2002.
- [46] A Doelman and R Schielen. Modulation equations for spatially periodic systems: Derivation and solutions. *SIAM Journal on Applied Mathematics*, 58(6):1901–1930, 1998.
- [47] L Korzinov, MI Rabinovich, and LS Tsimring. Symmetry breaking in nonequilibrium systems: Interaction of defects. *Physical Review A*, 46(12):7601, 1992.



## BIBLIOGRAPHY

---

- [48] R Manor, A Hagberg, and E Meron. Wave-number locking in spatially forced pattern-forming systems. *EPL (Europhysics Letters)*, 83(1):10005, 2008.
- [49] Rotem Manor, Aric Hagberg, and Ehud Meron. Wavenumber locking and pattern formation in spatially forced systems. *New Journal of Physics*, 11(6):063016, 2009.
- [50] Ehud Meron. Pattern-formation approach to modelling spatially extended ecosystems. *Ecological Modelling*, 234:70–82, 2012.
- [51] E Gilad, J Von Hardenberg, A Provenzale, M Shachak, and E Meron. A mathematical model of plants as ecosystem engineers. *Journal of Theoretical Biology*, 244(4):680–691, 2007.
- [52] J Swift and Pierre C Hohenberg. Hydrodynamic fluctuations at the convective instability. *Physical Review A*, 15(1):319, 1977.
- [53] J Lega, JV Moloney, and AC Newell. Swift-hohenberg equation for lasers. *Physical review letters*, 73:2978–2981, 1994.
- [54] Catherine Crawford and Hermann Riecke. Oscillon-type structures and their interaction in a swift–hohenberg model. *Physica D: Nonlinear Phenomena*, 129(1):83–92, 1999.
- [55] Golan Bel, Aric Hagberg, and Ehud Meron. Gradual regime shifts in spatially extended ecosystems. *Theoretical Ecology*, 5(4):591–604, 2012.
- [56] GA Worrall. Patchiness in vegetation in the northern sudan. *The Journal of Ecology*, pages 107–115, 1960.
- [57] LP White. Brousse tigrée patterns in southern niger. *The Journal of Ecology*, pages 549–553, 1970.
- [58] F Borgogno, P D’Odorico, F Laio, and L Ridolfi. Mathematical models of vegetation pattern formation in ecohydrology. *Reviews of Geophysics*, 47(1), 2009.



## BIBLIOGRAPHY

---

- [59] Vincent Deblauwe, Nicolas Barbier, Pierre Couteron, Olivier Lejeune, and Jan Bogaert. The global biogeography of semi-arid periodic vegetation patterns. *Global ecology and biogeography*, 17(6):715–723, 2008.
- [60] Christian Valentin, Jean-Marc d’Herbès, and Jean Poesen. Soil and water components of banded vegetation patterns. *Catena*, 37(1):1–24, 1999.
- [61] David John Tongway, Christian Valentin, and Josiane Seghieri. *Banded vegetation patterning in arid and semiarid environments: ecological processes and consequences for management*. Springer Verlag, 2001.
- [62] René Lefever and Olivier Lejeune. On the origin of tiger bush. *Bulletin of Mathematical Biology*, 59(2):263–294, 1997.
- [63] Christopher A Klausmeier. Regular and irregular patterns in semiarid vegetation. *Science*, 284(5421):1826–1828, 1999.
- [64] Reinier HilleRisLambers, Max Rietkerk, Frank van den Bosch, Herbert HT Prins, and Hans de Kroon. Vegetation pattern formation in semi-arid grazing systems. *Ecology*, 82(1):50–61, 2001.
- [65] Tomoo Okayasu and Yoji Aizawa. Systematic analysis of periodic vegetation patterns. *Progress of Theoretical Physics*, 106(4):705–720, 2001.
- [66] J Von Hardenberg, E Meron, M Shachak, and Y Zarmi. Diversity of vegetation patterns and desertification. *Physical Review Letters*, 87(19):198101, 2001.
- [67] Max Rietkerk, Maarten C Boerlijst, Frank van Langevelde, Reinier HilleRisLambers, Johan van de Koppel, Lalit Kumar, Herbert HT Prins, and André M de Roos. Self-organization of vegetation in arid ecosystems. *The American Naturalist*, 160(4):524–530, 2002.
- [68] Olivier Lejeune, Mustapha Tlidi, P Couteron, et al. Localized vegetation patches: a self-organized response to resource scarcity. *PHYSICAL REVIEW-SERIES E*, 66(1; PART 1):010901–R, 2002.



## BIBLIOGRAPHY

---

- [69] NM Shnerb, P Sarah, H Lavee, and S Solomon. Reactive glass and vegetation patterns. *Physical review letters*, 90(3):038101, 2003.
- [70] Moshe Shachak, Menachem Sachs, and Itshak Moshe. Ecosystem management of desertified shrublands in Israel. *Ecosystems*, 1(5):475–483, 1998.
- [71] Ehud Meron, Hezi Yizhaq, and Erez Gilad. Localized structures in dryland vegetation: forms and functions. *Chaos: An Interdisciplinary Journal of Nonlinear Science*, 17(3):037109–037109, 2007.
- [72] Assaf Y Kletter. *Dynamics of Vegetation Patterns in Water-limited Systems*. PhD thesis, Ben-Gurion University of the Negev, 2010.
- [73] Eusebius J Doedel. Auto: A program for the automatic bifurcation analysis of autonomous systems. *Congr. Numer*, 30:265–284, 1981.
- [74] Yair Mau, Aric Hagberg, and Ehud Meron. Spatial periodic forcing can displace patterns it is intended to control. *Physical Review Letters*, 109(3):034102, 2012.
- [75] Peter B Kahn and Yair Zarmi. *Nonlinear Dynamics: Exploration through Normal Forms*, volume 1. Wiley New York, 1998.
- [76] James E Byers, Kim Cuddington, Clive G Jones, Theresa S Talley, Alan Hastings, John G Lambrinos, Jeffrey A Crooks, and William G Wilson. Using ecosystem engineers to restore ecological systems. *Trends in Ecology & Evolution*, 21(9):493–500, 2006.
- [77] Richard J Hobbs and Viki A Cramer. Restoration ecology: interventionist approaches for restoring and maintaining ecosystem function in the face of rapid environmental change. *Annual Review of Environment and Resources*, 33:39–61, 2008.
- [78] David J Eldridge, Eli Zaady, and Moshe Shachak. Microphytic crusts, shrub patches and water harvesting in the negev desert: the shikim system. *Landscape Ecology*, 17(6):587–597, 2002.



## BIBLIOGRAPHY

---

- [79] Steward TA Pickett, Moshe Shachak, Bertrand Boeken, and Juan J Armesto. 2 the management of ecological systems. *Arid Lands Management: Towards Ecological Sustainability*, page 8, 1999.
- [80] Marten Scheffer and Stephen R Carpenter. Catastrophic regime shifts in ecosystems: linking theory to observation. *Trends in Ecology & Evolution*, 18(12):648–656, 2003.
- [81] SR Carpenter and WA Brock. Rising variance: a leading indicator of ecological transition. *Ecology letters*, 9(3):311–318, 2006.
- [82] Vasilis Dakos, Marten Scheffer, Egbert H van Nes, Victor Brovkin, Vladimir Petoukhov, and Hermann Held. Slowing down as an early warning signal for abrupt climate change. *Proceedings of the National Academy of Sciences*, 105(38):14308–14312, 2008.
- [83] Ryan A Chisholm and Elise Filotas. Critical slowing down as an indicator of transitions in two-species models. *Journal of theoretical biology*, 257(1):142–149, 2009.
- [84] Vishwesha Guttal and Ciriya Jayaprakash. Changing skewness: an early warning signal of regime shifts in ecosystems. *Ecology Letters*, 11(5):450–460, 2008.
- [85] Richard V. Craster and Roberto Sassi. Spectral algorithms for reaction-diffusion equations. 2006.